Journal of Membrane Science 713 (2025) 123388

Contents lists available at ScienceDirect

Journal of Membrane Science

journal homepage: www.elsevier.com/locate/memsci

Mixed matrix and thin-film nanocomposite membranes of PIM-1 and hydrolyzed PIM-1 with Ni- and Co-MOF-74 nanoparticles for CO_2 separation: Comparison of blending, grafting and crosslinking fabrication methods

Mustafa Alshurafa [a], Andrew B. Foster [a], Sulaiman Aloraini [a,b], Ming Yu [a,c], Boya Qiu [d], Patricia Gorgojo [d,e,f], Martin P. Attfield [a], Peter M. Budd [a,*]

[a] Department of Chemistry, School of Natural Sciences, The University of Manchester, Oxford Road, Manchester, M13 9PL, United Kingdom
[b] Department of Chemistry, College of Science and Arts, Qassim University, Ar Rass, 52571, Saudi Arabia
[c] Department of Chemical Engineering, The University of Melbourne, Melbourne, VIC, 3010, Australia
[d] Department of Chemical Engineering, Faculty of Science and Engineering, The University of Manchester, Manchester, M13 9PL, United Kingdom
[e] Instituto de Nanociencia y Materiales de Aragón (INMA), CSIC-Universidad de Zaragoza, Zaragoza, 50018, Spain
[f] Departamento de Ingeniería Química y Tecnologías del Medio Ambiente, Universidad de Zaragoza, C/ Pedro Cerbuna 12, 50009, Zaragoza, Spain

ARTICLE INFO

Keywords:
Polymer of intrinsic microporosity
Metal-organic framework
Mixed matrix membranes
Thin-film nanocomposites
Gas separation

ABSTRACT

The prototypical polymer of intrinsic microporosity, PIM-1, was synthesized with branched topology, then acid-hydrolyzed to introduce carboxylic acid functional groups (cPIM-1). Self-standing membranes and thin film nanocomposite (TFN) membranes were fabricated from PIM-1, cPIM-1, and Ni- or Co-MOF-74 nanoparticles (NPs), with a particular focus on TFNs for industrial viability. TFN membranes on polyacrylonitrile support were fabricated utilizing the following methods: (i) conventional blending; (ii) a grafting reaction between the hydroxyl group in the MOF-74 NPs and fluoro-groups of the chain-ends during PIM-1 synthesis; and (iii) an in-situ cross-linking reaction between the carboxylic acid groups in cPIM-1 and the metal ions of MOF-74 synthesized in-situ. Both conventional blending and grafting of PIM-1 with MOF-74 showed significant increase in permeance in TFN membranes. A grafted PIM-1 TFN membrane produced a CO_2 permeance of 9600 GPU, which is roughly 170 % higher than a pristine PIM-1 thin film composite (TFC) membrane, while also improving the selectivity. After 28 days of aging, a blended TFN membrane based on PIM-1 showed a CO_2 permeance of 1000 GPU and selectivities of 20.0 and 20.5 for CO_2/N_2 and CO_2/CH_4, respectively. Crosslinked cPIM-1 TFNs showed significant improvement in ideal selectivity from 65 in cPIM-1 to over 90 for CO_2/N_2, with permeance almost unchanged after crosslinking with Ni-MOF-74. However, small differences in the polyacrylonitrile support can result in significant changes in gas separation behavior. In mixed gas conditions, crosslinked cPIM-1/Co-MOF-74 produced an impressive 1842 GPU and CO_2/N_2 selectivity of 33. These results fall within the performance range that is suitable for post-combustion carbon capture.

1. Introduction

Cost-effective gas separation technologies for carbon capture are essential to minimize the effects of global warming. Excessive use of fossil fuels, to fulfil increasing demands as the world's population continues to grow, is the principal driver of rising global emissions [1–4]. Membranes are among the emerging technologies to overcome some of the challenges posed by conventional separation methods, offering low energy consumption, scalability, compactness, and simplicity of operation. In particular, polymeric membranes are attractive because of their low cost and ease of production [5,6].

Polymers of Intrinsic Microporosity (PIMs) are a class of microporous materials with pore sizes <2 nm that were first reported by Budd et al. in 2004 [7]. These polymers benefit from a rigid and contorted backbone, and thus inefficient packing, resulting in high free volume. The prototypical PIM, referred to as PIM-1, is solution-processable in commercial

* Corresponding author.
E-mail address: peter.budd@manchester.ac.uk (P.M. Budd).

https://doi.org/10.1016/j.memsci.2024.123388
Received 8 August 2024; Received in revised form 16 September 2024; Accepted 3 October 2024
Available online 5 October 2024

solvents such as chloroform and tetrahydrofuran (THF), and can be formed into self-standing membranes [8]. PIM-1 membranes exhibit high gas permeability and reasonable selectivity for industrial gas separation, especially for post-combustion (CO_2/N_2) processes [9]. Polymeric membranes, in general, suffer from a trade-off in permeability and selectivity, where an increase in permeability is usually associated with a decrease in selectivity and vice versa. This relationship is illustrated by the Robeson upper bound, which was first introduced in 1991 [10]. The main issues with membranes based on glassy polymers, such as PIMs, are physical aging and plasticization. Recent work by Yu et al. [11] showed that hydrolysis of PIM-1 to introduce carboxylic acid groups (cPIM-1) could retard aging, however, CO_2 induced plasticization is still a challenge that needs to be addressed. One approach is through the addition of filler particles to the polymer phase to fabricate mixed matrix membranes (MMMs) [12]. Fillers used in MMMs include metal-organic frameworks (MOFs) [13] and covalent organic frameworks [14], to benefit from their molecular sieving properties [15]. Recent work by Pu et al. [16] has shown that the correct fabrication of MMMs with PIM-1 can mitigate CO_2 induced plasticization.

MOFs are crystalline, porous materials constructed from metal clusters and organic linkers. They have potential for applications in gas separation and storage, adsorption, electrocatalysis and drug delivery systems, due to their high surface area and high porosity [17,18]. MOFs are structurally versatile and can be tuned for specific applications by adjusting the pore size, functionality, and thermal stability [19,20]. In gas separation, MOF-74 has attracted special attention due to its high CO_2 uptake and surface area, with excellent thermal and chemical stability. Mg-MOF-74 has attracted particular interest because it exhibits high CO_2 uptake and adsorption capacity. Other metal centres, such Ni, Co and Zn, have also been investigated for other applications [21–23]. Typically, conventional micron-sized MOF-74 is synthesized through a solvothermal synthesis route [24].

The incorporation of MOFs or other fillers in MMMs can enhance molecular transport and boost the separation performance [25,26], and can also help slow physical aging of polymeric membranes [27]. However, the majority of current MMMs are still below the targeted permeance and selectivity ranges introduced by Merkel et al. [28], who suggested that the optimum range for industrial post-combustion CO_2 separation is a CO_2 permeance of more than 1000 GPU and CO_2/N_2 selectivity greater than 20. Challenges encountered in the fabrication of MMMs include poor interactions between polymer and filler, leading to rigidification, interfacial voids or clogged pores, and the agglomeration of filler particles, which results in an uneven distribution across the membrane [29]. Therefore, highly selective gas separation depends largely on the compatibility between the two phases [30].

The majority of work on MMMs, and membranes in general, has been carried out on membranes with thicknesses in the range of tens of micrometres, which is unrealistic for industrial application due to the low fluxes that are achieved. Recent research has focused on thin film composite (TFC) membranes, with a thin (a few micrometres or less) selective layer on a porous support [11,25,31,32]. If filler materials are to be introduced, they need to be synthesized in the low nanoscale range, in order to fabricate thin film nanocomposite (TFN) membranes. TFC and TFN membranes provide numerous advantages, including high gas permeance and selectivity for CO_2/N_2 and CO_2/CH_4 from the thin active layer, with increased mechanical strength and durability provided by the porous support. TFCs are cost-effective, requiring only minimal amounts of material, and can be easily designed and scaled to fit different modular configurations for industrial applications.

Recent studies of MMMs have utilized chemical crosslinking and functional groups to enhance the dispersion and interfacial interactions, and thus overall performance of these membranes [33–35]. Lee et al. [15] crosslinked 6FDA-DAM with UiO-66 chemically for C_3H_6/C_3H_8 separation, giving enhanced interfacial compatibility between the two phases. These crosslinked MMMs also showed improved selectivity, as well as enhanced plasticization resistance at high pressure compared to neat polymer [15]. However, one concern with crosslinking is the change in transport and structural activity of the associated MOF [36]. A recent study by Lee et al. [37] presented a different fabrication strategy by utilizing cPIM-1 as a ligand to coordinate with different metals to form polymer-MOF MMMs, resulting in enhanced compatibility, dispersion and performance.

The aim of the present work was to compare different approaches for combining PIMs with MOFs, both as self-standing MMMs and as industrially more relevant TFN membranes. For the polymer phase, branched versions of PIM-1 and its hydrolyzed derivative cPIM-1 were employed. The MOFs used were Ni-MOF-74 and Co-MOF-74. The first approach involved conventional blending of pre-formed polymer and MOF. The second approach, grafting [38], involved covalently bonding polymer chains to the MOF particles by polymerization of the polymer in the presence of the MOF NPs, so that end groups (-F) of the polymer link to the reactive group of MOF-74 (-OH). The third approach was crosslinking, which involved covalently bonding a reactive side group (-COOH) on the polymer with the metal nodes (Ni or Co) of MOF-74 to create a crosslinked structure. For TFN membranes, three different polyacrylonitrile (PAN) supports were employed in this work, highlighting the influence of the support on membrane performance. Pure and mixed gas permeation measurements were carried out with N_2, CH_4, and CO_2. The fabricated TFC and TFN membranes in this work provide high permeance and good selectivity, with mechanical strength provided by the PAN porous support. In particular, the crosslinked TFN membranes with MOF NPs showed high potential for limiting the effect of plasticization in PIM-1 and cPIM-1 in mixed gas conditions.

2. Experimental

2.1. Materials

5,5′,6,6′-Tetrahydroxy-3,3,3′,3′-tetramethyl-1,1′-spirobisindane (TTSBI, 97 %) was purchased from Alfa Aesar and underwent purification prior to its use in the synthesis of PIM-1, following the procedure described below. Tetrafluoroterephthalonitrile (TFTPN, >99 %) was purchased from Fluorochem. Anhydrous potassium carbonate (K_2CO_3) was purchased from Fisher Scientific Ltd., ground to a fine powder and dried in a vacuum oven before usage. Nickel acetate tetrahydrate ($Ni(CH_3COO)_2{\cdot}4H_2O$, 99 %), cobalt acetate tetrahydrate ($Co(CH_3COO)_2{\cdot}4H_2O$, 99 %) and 2,5-dihydroxyterephthalic acid (H_4DHTP, 97 %) were purchased from Alfa Aesar and used as received. N,N-Dimethylformamide (DMF) was purchased from Fisher Scientific. N,N-dimethylacetamide (DMAc, 99.8 %), toluene (≥99.7 %), chloroform stabilized in amylene (HPLC, ≥99.8 %), chloroform stabilized in ethanol for GPC analysis (≥99.8 %), tetrahydrofuran (THF, ≥99.8 %), methanol (≥99.8 %), anhydrous 1,4-dioxane (99.8 %), ethyl acetate (GC, ≥99.5 %), hexane (HPLC, ≥97 %) and $CDCl_3$ were purchased from Sigma-Aldrich. Sepro PA350 polyacrylonitrile (PA350) ultrafiltration membrane support was provided by Prof. Ingo Pinnau, KAUST and R&DC, Saudi Aramco. UF 010104-1501 batch of polyacrylonitrile support was purchased from Solsep (The Netherlands). Solecta support was kindly provided from R&DC, Saudi Aramco. For the purification of TTSBI monomer, 40 g was placed in a three-neck round-bottom flask (3 L) equipped with a nitrogen flow inlet and reflux condenser. Ethyl acetate (667 mL) was added to the flask, and the solution was refluxed at 90 °C. The mixture was allowed to reflux until the dissolution of the monomer was complete. Hexane (667 mL) was added to the flask and allowed to stir for an additional 10 min. The flask was subsequently removed, allowed to cool to room temperature, and placed in an ice bath for 3 h. Finally, the product was filtered and placed in a vacuum for 24 h to dry for use in PIM-1 synthesis.

2.2. Synthesis and purification of PIM-1

Three different PIM-1 samples were synthesized using a modified

version of the high temperature method [39]. The reaction scheme is shown in Fig. S1. TTSBI (17.02 g, 0.05 mol), TFTPN (10.00 g, 0.05 mol) and K_2CO_3 (20.73 g, 0.150 mol) were placed into a 500 mL three-neck round bottom flask. A solvent mixture of DMAc (120 mL) and toluene (60 mL) was added to the flask, which equates to 20 % excess solvent mixture compared to the conventional high temperature method [40, 41]. The initial use of extra solvent at the start slows down the temperature ramping rate, resulting in PIM-1 with increased branching compared to conventional methods. The flask was then placed on a DrySyn heating block (Asynt, UK) over a hot plate magnetic stirrer (IKA, UK). The flask was connected to a nitrogen flow, an RZR mechanical stirrer (with digital rpm, torque, and time readings), and a condenser. The mixture was heated to 160 °C while monitoring the temperature profile. Mechanical stirring was set at 250 rpm and adjusted throughout the reaction, depending on the change in viscosity of the solution mixture. Additional amounts of DMAc (20 mL) and toluene (10 mL) were added to reduce the overall viscosity of the solution at 27 and 36 min. The reaction was stopped after 45 min and quenched with excess of methanol.

The recovered polymer was collected by a sintered glass filter. For polymer purification, the collected product was first re-dissolved in chloroform (at a concentration of 5 g per 120 mL) until completely dissolved. The dissolved polymer was then re-precipitated slowly into methanol, and then collected via filtration once again. PIM-1 was then refluxed in deionized water overnight (16 h) and collected by vacuum filtration. The polymer was immersed in a minimal amount of 1,4-dioxane for 15 min, then washed with excess amounts of acetone and methanol. The polymer was left overnight in methanol to remove all traces of other solvents. Finally, the filtered polymer was dried in a vacuum oven at 120 °C for a few days.

2.3. Synthesis and purification of acid hydrolyzed PIM-1 (cPIM-1)

Acid hydrolysis was carried out on B-PIM-1b and B-PIM-1c based on a method published by the Smith group [42]. The reaction scheme is shown in Fig. S2. In this scaled up method, 2.4 g of PIM-1, 144 mL of de-ionised water, 144 mL of sulfuric acid and 48 mL of glacial acetic acid were added to a 1 L round-bottom flask. The flask was placed in a DrySyn heating block on top of a hot plate magnetic stirrer with a water condenser attached to the flask. The reaction was left to stir at 160 °C for 6 h, 12 h or 24 h, depending on the desired conversion. The reaction was then stopped, cooled down to room temperature, and diluted in 4 L of deionized water. The carboxylic acid-functionalized PIM-1 (cPIM-1) was collected through vacuum filtration. The product was then refluxed in slightly acidic (with a few drops of sulfuric acid) deionized water for 16 h. The final modified product was collected by a sintered glass filter funnel via vacuum filtration and dried in a vacuum oven overnight before use.

2.4. Synthesis and purification of M-MOF-74 (M = Ni or Co) nanoparticles

M-MOF-74 (M = Ni or Co) was synthesized based on a method published by Díaz-García et al. [24]. The reaction scheme is shown in Fig. S3. A solution of 2,5-dihydroxyterephthalic acid (0.200 g, 1.00 mmol) dissolved in DMF (5.00 g) was added dropwise to a solution of metal (Ni or Co) acetate tetrahydrate (2.60 mmol) in DMF (5.00 g) in a 50 mL round bottom flask. The addition of the organic linker resulted in immediate formation of M-MOF-74. The reaction was allowed to proceed for 20 h, and the product was collected by centrifugation. The collected MOF-74 nanoparticles were purified by washing and immersing in methanol (20 mL) three times over a period of six days to completely remove DMF from the final product. The final product was stored in a vacuum oven for 2 days at 120 °C.

2.5. Grafting of M-MOF-74 (M = Ni or Co) with PIM-1

A grafting reaction was carried out during PIM-1 polymerization in the presence of pre-synthesized Ni or Co-MOF-74 nanoparticles. The proposed grafting mechanism is shown in Fig. 1. TTSBI (1.702 g, 5.000 mmol), TFTPN (1.00 g, 5.00 mmol) and potassium carbonate (2.073 g, 15.0 mmol) were placed into a 100 mL three-neck round bottom flask along with Ni-MOF-74 or Co-MOF-74 (0.23 g, 10 % w/w). A mixture of 12 mL of DMAc and 6 mL of toluene was added to the round bottom flask. The flask was placed in a DrySyn aluminum heating block on a hot plate. The three-neck flask was connected to a nitrogen flow, mechanical stirrer, and condenser. The reaction mixture was heated from room temperature to 160 °C, with mechanical stirring initially set at 200 rpm. The stirring rate was raised to a maximum of 350 rpm throughout the reaction, as the viscosity of the mixture increased. The hot viscous reaction mixture was quenched into methanol after 45 min, precipitating as threads of green/yellowish colored product. The product was purified following the procedure described above for PIM-1. The yield was calculated to be 95 % and 94 % for PIM-1/Ni- and Co-MOF-74, respectively.

2.6. Crosslinking of cPIM-1 by in-situ synthesis of Ni/Co-MOF-74 NPs

The proposed reaction scheme for crosslinking is shown in Fig. 2. For crosslinking of self-standing membranes in the solid state, cPIM-1 membrane (0.303 g, 0.602 mmol) was placed in a large glass Petri dish. Nickel or cobalt acetate tetrahydrate (3 mg, 0.012 mmol) was dissolved in 3 mL of methanol. This equates to 8 mol % of metal salt per carboxylic acid group in cPIM-1 present in the mass of the film (experiments with higher mol % were also carried out). The metal solution was then added to the Petri dish, and left to react for 30 min. Then, 2,5-dihydroxyterephthalic acid (1 mg, 0.005 mmol) was dissolved in methanol, and added to the Petri dish. The crosslinking reaction was allowed to carry on for 24 h, and then the clear methanol supernatant was removed. A change of colour in the crosslinked membrane was observed, from brown to green for nickel and to almost red for cobalt-based membrane. The membrane was then washed three times with methanol to remove any unreacted materials. The final film was left in a N_2 cabinet overnight, and then 24 h in vacuum oven at 120 °C to remove any traces of solvents. To confirm crosslinking, the film was washed with THF two times, where no cPIM-1 leaching was observed (the film was completely insoluble, and no significant visual change in structure of film was observed).

For thin film fabrication, cPIM-1-60% (0.400 g, 0.808 mmol) was dissolved in THF (10 mL) in a 50 mL round bottom flask. Nickel or cobalt acetate tetrahydrate (3.5 mg, 0.014 mmol) was dissolved in 1 mL of methanol and then slowly added to the cPIM-1 solution, resulting in the formation of a suspension. This equated to about 3 mol % of metal salt per carboxylic acid group of cPIM-1 present in the mass of the film. Then, 2,5-dihydroxyterephthalic acid (1 mg, 0.005 mmol) was dissolved in methanol and added dropwise to the solution. The reaction was then left to stir at room temperature overnight. The solution went back to visually looking like a homogenous solution the next day, which was suitable for the TFC membrane kiss-coating method. The solution was then used as a coating solution on PAN support following the procedure described below.

2.7. Membrane fabrication

2.7.1. Self-standing membranes

Solutions of PIM-1 and cPIM-1 were prepared by dissolving 0.15 g of the polymer in 5 mL of chloroform and THF, respectively. The solution was filtered through glass wool to remove any impurities, then cast on a PTFE Petri dish. The Petri dish was covered with a glass dish and placed in a N_2 cabinet for 3 days at room temperature to allow the solvent to evaporate. The self-standing membrane was placed in a vacuum oven for 24 h at

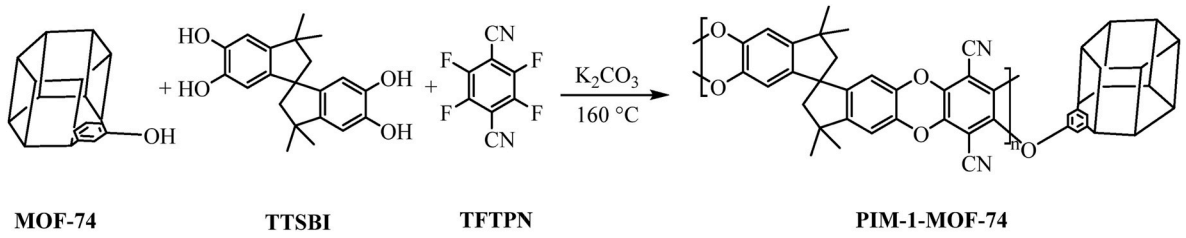

Fig. 1. Proposed grafting mechanism for PIM-1 with M-MOF-74 (M = Ni or Co) nanoparticles in DMAc/toluene (2:1) solvent system.

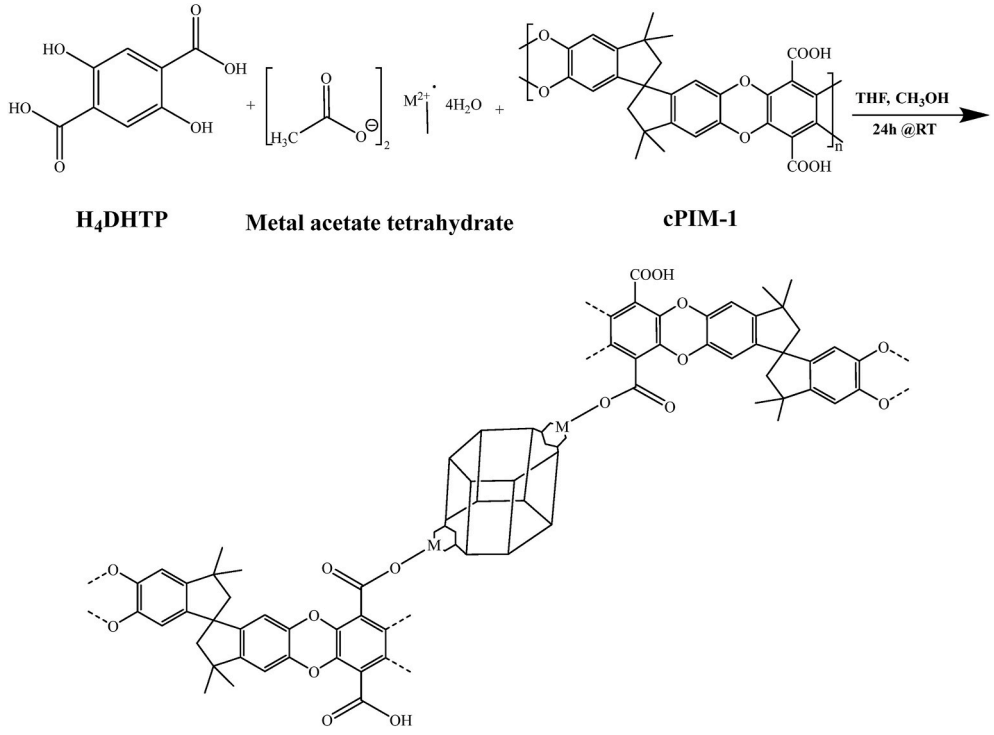

Fig. 2. Proposed in-situ crosslinking mechanism for cPIM-1 with M-MOF-74 (M = Ni or Co) nanoparticles.

120 °C to completely remove all traces of solvents. The film thicknesses were measured using a micrometer (Mitutoyo, Japan). Self-standing membranes of PIM-1 and MOF-74 blends were prepared by dissolving 0.20 g of PIM-1 in 5 mL chloroform, then 5 % w/w of MOF-74 was added to the solution, followed by mechanical stirring and ultrasonication bath (Branson 2510MTH, USA) for 6 h. Self-standing membranes of grafted samples were prepared by simply dissolving 0.20 g of the materials in 5 mL of chloroform, followed by casting as described above.

2.7.2. Thin film composite and nanocomposite membranes

TFC and TFN membranes were prepared using a kiss-coating method on PAN supports from different suppliers [40,43]. The coating solutions of PIM-1 and cPIM-1 samples were prepared at concentrations of 3 % and 4 % w/v in chloroform and THF, respectively. The coating solutions of PIM-1 and MOF-74 blends were prepared by dissolving 0.3 g of PIM-1 in 10 mL chloroform, then 5 % w/w of MOF-74 was added to the solution, followed by mechanical stirring and ultrasonication bath for 6 h. Grafted samples were prepared by dissolving 0.3 g of PIM-1/Ni or Co-MOF-74 in 10 mL of chloroform. PAN support was cut to a 4 cm × 9 cm size suitable for the roller-coater wheel used in the laboratory. The support sheets were sealed with aluminium tape on all edges to prevent contact of the polymer solution with the back of the support. A programmable DC power supply motor (RS-3005P, RS PRO, UK) was used for coating, set at 15 V and a current of 0.15 A. The support came into contact with the casting solution for one full rotation (about 4 s). Relative height between coating solution, roller wheel, and coating volume during kiss-coating were kept consistent across all samples for reproducible results. The resulting membranes were kept in a nitrogen cabinet for 24 h, then tested for their performance.

2.8. Gas permeation measurements

2.8.1. Single gas testing

Single gas permeation measurements for all fabricated membranes were performed using pure N_2, CH_4 and CO_2 by the standard variable volume method [44,45]. Samples were mounted and cut into a suitable size for the permeation cell (active membrane area of 2.84 cm^2). The upstream gauge pressure was maintained at 2.5 atm and room temperature, while the downstream permeate was kept at atmospheric pressure. The samples were conditioned for 5 min for TFC and TFN membranes, and for 20 min for self-standing membranes. Upon conditioning, gas permeation measurements were performed for 15 min, and time is recorded for a specified volume of gas through the membrane. Three different membranes were tested for each type of sample and the

average is reported. The gas permeance for all membranes was calculated using equation (1):

$$K = \frac{Q \times 10^6}{tA(p_a - p_b)} \quad (1)$$

where K is the permeance in GPU, where 1 GPU $= 10^{-6}$ cm^3 (STP) cm^{-2} s^{-1} cmHg^{-1} $= 3.348 \times 10^{-10}$ mol m^{-2} s^{-1} Pa^{-1}. Q is the volume at STP of the gas permeated in cm^3, t is the permeation time in seconds, A is the active membrane area in cm^2, p_a and p_b are the pressures (in cmHg) from the upstream and permeate sides, respectively. Membrane permeability can be calculated using equation (2):

$$P = K \times l \quad (2)$$

where P is the permeability in Barrer, where 1 Barrer $= 10^{-10}$ cm^3(STP) cm cm^{-2} s^{-1} cmHg^{-1} $= 3.348 \times 10^{-16}$ mol m m^{-2} s^{-1} Pa^{-1}, and l is the thickness of the membrane in micrometres. Membrane ideal selectivity is calculated as the ratios of permeances or permeabilities, as expressed by equation (3):

$$\alpha_{CO_2/x} = \frac{P_{CO_2}}{P_x} \quad (3)$$

where α is the ideal selectivity, P_{CO_2} is the permeability of CO_2 and P_x is the permeability of N_2 or CH_4.

2.8.2. Mixed gas testing

Mixed gas measurements for cPIM-1 and crosslinked cPIM-1 with Ni- and Co-MOF-74 were performed with binary mixtures of 50 % CO_2/50 % N_2 and 50 % CO_2/50 % CH_4 at 50 SCCM with feed pressure set to around 2.5 bar at room temperature and the permeate side pressure set to approximately 1.07 bar. The permeate was analyzed with an automated gas chromatograph (GC, Agilent Technologies 490) equipped with 10 m PoraPLOT U (PPU) heated Column, with a thermal conductivity detector (TCD) for CO_2, CH_4, and N_2 detection. Mixed gas permeance was calculated using the standard variable method using equation (4):

$$K_i = \frac{Qy \times 10^6}{tA(p_a x - p_b y)} \quad (4)$$

where K_i is the permeance of CO_2, CH_4 or N_2 in GPU, while x is the mole fraction on the feed side and y is the mole fraction on the permeate side. Q, t, A, p_a and p_b are defined above. Mixed gas selectivity is calculated as the ratio of permeances.

2.9. Characterization Techniques

Gel permeation chromatography was utilized to measure number-average molar mass (M_n), weight-average molar mass (M_w), and dispersity ($Đ$) of PIM-1. Samples were prepared at a concentration of 1 mg ml^{-1} in chloroform (stabilized in ethanol). The samples were then examined using a triple detector Viscotek VE2001 system (Malvern Panalytical, UK) at a flow rate of 1 mL min^{-1} at 30 °C and an injection volume of 100 μL through two PL mixed-B columns. The data were collected by OmniSec software.

Proton Nuclear Magnetic Resonance (^{1}H NMR) was recorded using a Bruker Avance II 500 MHz instrument. PIM-1 and cPIM-1 polymers were dissolved in $CDCl_3$ and DMSO-d_6, respectively, at concentrations of 20 mg mL^{-1}.

Elemental (C, H & N) analysis was performed using a Thermo Flash 2000 CHN&S analyzer (Thermo Scientific, The Netherlands). Metal analysis for Ni and Co was conducted by inductively coupled plasma atomic emission spectroscopy (ICP-AES) iCAP 6300 Duo (Thermo Scientific).

Thermogravimetric analysis (TGA) was analyzed by a PerkinElmer TGA/DSC 8000 system. The sample was heated from room temperature to 600 °C at a rate of 10 °C min^{-1} under N_2 atmosphere. These results were used to determine the conversion of –CN to –COOH in PIM-1 hydrolysis.

Powder X-ray diffraction (PXRD) was utilized using a Philips X'pert X-ray diffractometer (40 kV and 30 mA) to analyze the synthesized MOF nanoparticles, grafted and crosslinked samples. The samples were ground to a fine powder form, then placed on the XRD measurement plate. Each measurement was performed at 2θ from 3 to 40° at a speed of 1° min^{-1}. The data were collected by X'pert Philips Highscore Plus. Mercury software was utilized to compare experimental results with CSD database for micro-sized MOF-74 of nickel and cobalt. An estimation of particle size was calculated from PXRD peak broadening using the Scherrer equation. This is important here due to aggregation and agglomeration of nanoparticles in general, and particularly observed in Ni and Co-based MOF-74 [24]. The Scherrer equation is defined by equation (5):

$$\tau = \frac{K\lambda}{\beta \cos\theta} \quad (5)$$

where τ is the mean size of the crystalline domains, which may be smaller or equal to the particle size. K is a constant with a factor of 0.9, λ is the x-ray wavelength, β is the line broadening at half the maximum intensity and θ is the Bragg angle.

Dynamic light scattering (DLS) was utilized to analyze particle sizes of polymers and MOF-74 samples in different solvents, chloroform, THF, and methanol. The dispersed solutions were measured at a concentration of 50 ppm at 25 °C using a Malvern Zetasizer Nano ZS instrument.

Fourier Transform Infrared Spectroscopy (FTIR) was carried out using a Vertex 70 FTIR instrument at 128 scans and a resolution of 4 cm^{-1}. Each sample was ground to a fine powder for the analysis. Data were analyzed using OPUS software.

FEI Quanta 250 ESEM (equipped with SE, BSE and EDS detectors) was utilized to obtain morphological information about MOFs and polymer samples. The samples were ground and scattered over carbon tabs, mounted over the aluminum disc, and analyzed using secondary detector (SE) morphological information. For cross-sectional imaging, samples were cryo-snapped in liquid nitrogen for 15 s after being submerged in DI water for 15 s causing the membrane to fracture easily for a clear image. Using a Pd/Au Quorum Sputter (UK), 5 nm of Au:Pd (80:20) nanoparticles were coated to the membranes, which were then allowed to dry for 3 h. The images were generated by a Secondary Electron detector and analyzed using ImageJ® software. Energy dispersive X-ray spectroscopy (EDS) was carried out on crosslinked samples to confirm the incorporation of MOF-74 into the TFN membranes. Samples were analyzed using Aztec software.

For high-angle annular dark-field scanning transmission electron microscopy (HAADF-STEM) imaging, a FEI Talos F200A analytical electron microscope (AEM) was employed, operated at 200 kV. This setup was equipped with a Schottky field-emission gun (X-FEG) operating at an extraction voltage of 4.5 kV, a monochromator (energy spread 0.25 eV) and an FEI Super-X 4-detector energy dispersive X-ray (EDX) system. Membrane samples were first embedded in EpoThin 2 epoxy resin for 48 h. After curing, the resin block was trimmed into a pyramid-like shape using a glass knife on a Leica EM UC7 ultramicrotome, exposing the cross-section of the membrane. Ultrathin sections were then cut with a diamond knife set at a 6° angle, with the cutting speed adjusted to 1 mm/s. The sections were mounted on carbon 300 mesh copper grids for imaging.

3. Results and discussion

3.1. Synthesis and characterization of PIM-1 and cPIM-1

Three samples of PIM-1 with varying degrees of branching (Table 1) were synthesized and characterized for this work. Previous studies by Yu et al. [11] showed that a reduction in temperature in the early stages of polymerization could favour mono-substituted polymerization rather

Table 1
Polymerization conditions and characterization results for PIM-1 samples: Polymerization temperature, yield, branching, weight-average molar mass (M_w), number-average molar mass (M_n), dispersity ($Đ$) and intrinsic viscosity ([η]).

PIM-1 sample	Temperature Set/avg. (°C)	Yield (%)	Branching (%)	M_w (kg mol^{-1})	M_n (kg mol^{-1})	$Đ$	[η] (cm^3 g^{-1})
B-PIM-1a	160/125	92	6.8	186	118	1.6	46.0
B-PIM-1b	160/121	88	6.1	118	66.5	1.8	32.2
B-PIM-1c	160/131	95	7.9	152	69.7	2.2	41.8

than disubstituted polymerization, leading to branched structures. This was achieved here by marginally adjusting the polymerization temperature profile (Fig. S4), by adding 20 % extra solvent at the beginning of the reaction and at later stages during the synthesis (upon observation of a slight change in viscosity) [40,41]. The reaction was stopped once the viscosity increased significantly. The main evidence of branching comes from the ^{1}H NMR spectrum in the aromatic region. An example of a branched sample is shown in Fig. S5. PIM-1 exhibits two main aromatic resonances at 6.74 and 6.35 ppm (a and b), while minor peaks at 6.60 and 6.18 ppm (c and d) are associated with branched structures [41]. The degree of branching as a percentage of all PIM-1 residues was calculated using Lorentz fitting based on a method published elsewhere [41]. Lorentz fitting and branching calculations are included in the SI (Figs. S10–S12 and Table S1). PIM-1 was hydrolyzed to cPIM-1 to change the polymer functionality from –CN to –COOH, which gives membranes with higher ideal selectivity [11,42]. Upon hydrolysis of PIM-1 for 24 h, a peak in ^{1}H NMR was observed at 13.8 ppm, which is associated with the carboxylic acid proton in cPIM-1, as shown in Fig. S5. ^{1}H NMR spectra of PIM-1 and cPIM-1 used in this study are included in the Supplementary Information (SI), Figs. S6–S9.

Multi-detector gel permeation chromatography (GPC) analysis of the PIM-1 samples (Table 1) indicated weight-average molar masses (M_w) ranging from 118 to 186 kg mol^{-1} and dispersities ($Đ = M_w/M_n$) ranging from 1.6 to 2.2. B-PIM-1a, B-PIM-1b and B-PIM-1c have branching percentages of 6.8 %, 6.1 % and 7.9 %, respectively. Branching can have a significant impact on gas separation performance and physical aging, thus it is important to utilize branched PIM-1 in MMM fabrication for optimum performance. cPIM-1 was not analyzed by GPC due to possible interactions with the GPC columns. However, dynamic light scattering (DLS) analysis was carried out to provide comparison between the hydrodynamic diameter before and after hydrolysis. Number distributions of hydrodynamic size from DLS (Fig. S13) indicate a slight shift to larger size on conversion from PIM-1 to cPIM-1. There was no evidence to indicate degradation or aggregation of the cPIM-1 samples in DLS analysis.

Elemental analysis (Table S2) was utilized to calculate the percentage conversion of –CN to –COOH on hydrolysis of PIM-1, which is important for film durability, performance and physical aging. Three hydrolyzed samples with 25 %, 60 % and 69 % conversion were utilized in this study for self-standing thick films, TFC and TFN membranes. FT-IR spectra of PIM-1 and cPIM-1b-60% are shown in Fig. S14. A sharp stretch at 2240 cm^{-1} for the nitrile (-CN) group is clearly present in the PIM-1 spectrum. After acid hydrolysis, the nitrile stretch diminishes, due to conversion from –CN to –COOH. Another noticeable difference is the rise in the carbonyl (–C═O) peak at 1721 cm^{-1} in the hydrolyzed PIM-1 sample.

3.2. Synthesis and characterization of M-MOF-74 (M = Ni or Co)

Ni- and Co-MOF-74 NPs were synthesized at room temperature based on a method published by Díaz-García et al. [24]. Powder XRD patterns of Ni- and Co-MOF-74 NPs are shown in Fig. S15. For comparison purposes, simulated micron-sized Ni-MOF-74 from the Cambridge Structural Database is included. Two main peaks for Ni-MOF-74 at around 2θ 6.84° and 11.84° can be detected. Broadening of major peaks in the synthesized samples serves as the primary evidence for the formation of MOF-74 nanocrystals in comparison to the simulated MOF-74 materials synthesized by solvothermal methods. Ni-MOF-74 shows more severe broadening compared to Co-MOF-74, which may indicate a smaller crystallite size. Estimation of crystallite sizes of Ni- and Co-MOF-74 through powder XRD peak broadening can be achieved using the Scherrer equation. From the obtained spectra, the crystallite sizes were calculated to be 2.4 nm and 3.5 nm for Ni-MOF-74 and Co-MOF-74, respectively.

Scanning electron microscopy (SEM) was utilized to measure the particle size and examine the morphology. Fig. S16 shows SEM images of the synthesized Ni and Co-MOF-74 samples after activation at 120 °C in a vacuum oven to remove any guest molecules. The average sizes of the nanoparticles of Ni-MOF-74 (Fig. S16a) and Co-MOF-74 (Fig. S16c) were measured to be 52 nm and 82 nm, respectively. Further SEM images are included in the SI (Fig. S17), which show agglomerates of MOF NPs. Vigorous magnetic stirring and ultrasonication were used during TFN membrane fabrication to minimize agglomeration, to obtain membranes with good dispersion of MOF. In DLS (Fig. S18) Ni- and Co-MOF-74 exhibited similar intensity and number distributions of particle size. The number-average hydrodynamic diameters of Ni-MOF-74 and Co-MOF-74 were determined to be 192 and 254 nm, respectively. This is mainly due to the agglomeration of the M-MOF-74 particles. Nanoscale MOF materials are especially prone to agglomeration [46]. These findings are in good agreement with literature findings [24]. Thermogravimetric analysis (TGA) profiles of Ni- and Co-MOF-74 (Fig. S19) show large losses of weight (20 %) from 50 to 150 °C, attributed to the removal of trapped DMF, CH_3OH, and possibly moisture [47]. From 300 to 600 °C, a second loss of weight of 37 % and 39 % is observed for Ni- and Co-MOF-74, respectively. This is attributed to the decomposition or collapse of the MOF-74 structure. Synthesized samples showed greater thermal stability than those reported by Díaz-García et al. [24], which may be attributed to the difference in characterization conditions by TGA or purity of the sample. In general, TGA results are in fair agreement with literature values for the synthesized M-MOF-74 [24,48]. These results provide good evidence along with XRD analysis to confirm that these are MOF-74 nanocrystals. Quantitative analysis of the TGA results is provided in Table S3.

3.3. Fabrication and characterization of mixed matrix and TFN membranes

Self-standing MMMs and thin film nanocomposite membranes were fabricated via three different approaches. The first approach involved conventional blending of B-PIM-1a solution with Ni- and Co-MOF-74 NPs, with vigorous stirring and ultrasonication for 6 h to minimize agglomeration and enhance dispersion of MOF-74 NPs. Initial studies via this approach on self-standing MMMs of PIM-1 (60–80 μm) with 5 wt % loading of M-MOF-74 (M = Ni or Co) exhibited limited robustness and durability. As the loading of MOF-74 NPs increased, the membranes became increasingly brittle, posing challenges for gas permeation measurements. Consequently, alternative approaches for incorporating the filler phase into the polymer matrix were explored. The second approach involved grafting MOF-74 NPs during polymerization of PIM-1 via hydroxyl groups in MOF-74 with fluorine atoms in PIM-1. The grafted MMMs were prepared in chloroform with stirring and ultrasonication. Grafted samples from PIM-1 showed enhancement in durability and dispersion of NPs compared to blended samples. The third approach involved crosslinking the hydrolyzed version of PIM-1 through the reactive carboxylic acid group with the metal acetate (Ni or Co).

As cast self-standing MOF-containing membranes (Fig. S20) with grafted PIM-1, and crosslinked samples with cPIM-1b, displayed more equally dispersed color compared to those obtained by conventional

blending methods. The in-situ crosslinked membranes were insoluble in THF and dimensionally stable after immersion, which is an indication of crosslinking. Change of color was also observed (Fig. S21) from dark brown to light green and pale red for cPIM-1/Ni-MOF-74 and cPIM-1/Co-MOF-74, respectively. Crosslinked self-standing membranes became more brittle as a result of crosslinking, in comparison with pristine PIM-1 or cPIM-1, posing challenges in pure gas permeation measurements. To minimize brittleness caused by hydrolysis, cPIM-1b with a low degree of hydrolysis (25 %) was used for self-standing membranes. Elemental analysis of grafted and crosslinked self-standing MMMs utilized in gas permeation experiments are presented in Table S4. Elemental analysis shows presence of both Ni and Co in the grafted membranes, which is most likely due to the presence of MOF-74 in the samples. However, higher amounts of Ni or Co in the grafted samples had been expected due to the higher initial loadings of MOF, which suggests some losses during purification of grafted polymer. The presence of both Ni and Co was also confirmed in crosslinked samples. The detected amounts of both Ni and Co closely align with the expected values in the self-standing crosslinked MMMs.

In TFN membrane fabrication, in general, challenges of brittleness and durability were minimized due to the mechanical strength provided by the PAN support, compared to self-standing MMMs. In the first and second approaches, solutions for fabricating TFN membranes were prepared using the same methodology as used for self-standing membranes. In the first approach, B-PIM-1a was utilized in blends coated on PAN support from Sepro PA350 and Solsep UF 010104-1501 (Solsep UF). For the second approach, grafted samples were also coated on both Sepro PA350 and Solsep UF. The third approach used cPIM-1b and cPIM-1c with 60 % and 69 % hydrolysis degree for ideal gas and mixed gas studies, respectively. This was primarily to achieve high permeance and selectivity as shown by Yu et al. [11]. Physical aging behavior can be optimized by the degree of hydrolysis, with more highly hydrolyzed PIM-1 aging more slowly due to increased hydrogen bonding. These samples were coated onto Sepro PA350 and Solecta PAN supports. The corresponding crosslinking reaction with the hydrolyzed PIM-1 was performed in solution through the introduction of metal acetate and organic linker, followed by coating the resulting solution on PAN support. The fabricated TFN membranes prepared from 4 % cPIM-1 primed with 3 mol% of metal acetate per carboxylic acid group unit on the cPIM-1 were found to be partially soluble (leaching was observed in TFN when immersed) in THF, while TFN membranes made from 4 % cPIM-1 and 12 mol% of M-MOF-74 were found to be insoluble in THF and no colour leaching was observed (Fig. S22). This was an indication of crosslinking in the TFN membrane. Visual evidence of crosslinking of cPIM-1b-60% with the metal acetate and organic linker in membranes immersed in THF is shown in Fig. S22. Crosslinking at levels of metal acetate equal or higher than 20 mol% per carboxylic acid unit in cPIM-1 was not advantageous as stronger interactions caused the formation of solid precipitate in coating solutions. It is also worth noting that when the metal node, $(M(OAc)_2)\cdot 4H_2O$, is introduced alone, gel-like material is formed at higher mol%.

Powder XRD of PIM-1, cPIM-1, M-MOF-74 (M = Ni or Co), grafted and crosslinked self-standing membranes are presented in Fig. 3. PIM-1 exhibits three peaks at 13.1°, 18.0° and 23.2°, whereas cPIM-1 exhibits three similar peaks but slightly shifted to the right at 13.7°, 18.5° and 23.4°. These peaks are attributed to spacings between loosely packed chains, micropores within the polymer and aromatic interactions, respectively [49]. By contrast, M-MOF-74 (M = Ni or Co) nanoparticles show two characteristic peaks at around 6.8° and 11.8° for Ni particles, and 7.2° and 11.7° for Co particles. In grafting, MOF-74 peaks are not

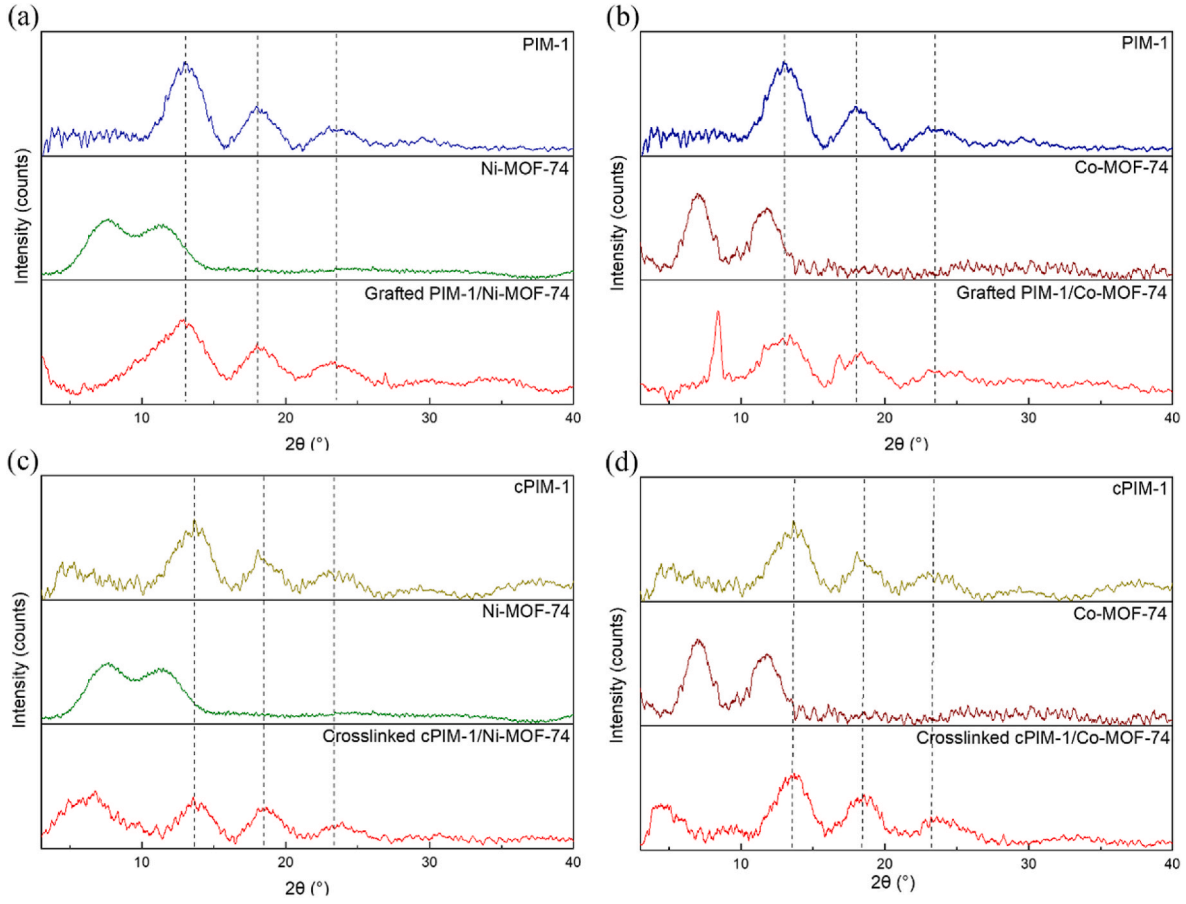

Fig. 3. Normalized PXRD spectra from self-standing membranes of (a) PIM-1, Ni-MOF-74 and grafted PIM-1/Ni-MOF-74 (10 %), (b) PIM-1, Co-MOF-74 and grafted PIM-1/Co-MOF-74 (10 %), (c) cPIM-1, Ni-MOF-74, crosslinked cPIM-1/Ni-MOF-74 (3 mol%), (d) cPIM-1, Co-MOF-74, crosslinked cPIM-1/Co-MOF-74 (3 mol%).

detected, which is possibly due to the broadening and high intensity of XRD peaks from non-crystalline PIM-1 overlapping MOF-74 XRD peaks. Additionally, the second and third polymer peaks in both Fig. 3a and **b** have shifted slightly to the right with increased broadness of the peaks, as well as a decrease in the intensity. The shift might be attributed to interactions between the polymer and MOF NPs drawing the polymer chains closer to each other [49]. The broadening and decrease in intensity may be due to the impact of nanocrystalline MOF in the sample [50]. In crosslinked samples (Fig. 3c and **d**), a more significant shift to the right for the three peaks in cPIM-1, along with slight decrease in intensity, was observed. This may be an indication of a stronger interaction between the polymer chains with the carboxylic acid group and MOF-74 (-OH) via hydrogen bonding. Additional peaks also appeared at 6.8° for Ni-based crosslinked samples, which closely matches the XRD pattern of the nanoMOF-74 peak. The second peak may be obscured by the presence of cPIM-1. In crosslinked Co-based samples, a peak appears at 4.7° that does not match the expected patterns for either the polymer or the MOF. This may be attributed to a secondary phase or may be a result of crosslinking between the cPIM-1 and metal acetate in the sample. XRD spectra with higher loading of MOF-74 in both grafted and crosslinked samples are presented in Fig. S23. These results confirm the presence of the MOF-74 phase in samples prepared using both grafting and crosslinking methods.

Fig. 4 shows the thermal decomposition profiles of PIM-1, cPIM-1, MOF-74 and grafted and crosslinked self-standing MMMs. Results for individual polymers (PIM-1 and cPIM-1) and M-MOF-74 (Ni or Co) mostly agree with literature [24,27]. The PIM-1 sample was thermally stable up to 530 °C, where the first weight loss occurs due to polymer backbone decomposition in the range of 530 °C–550 °C. Below 75 °C, grafted samples showed an initial loss of 8 %, possibly due to trapped methanol within the MOF structure, as MOF-74 NPs were introduced at the start of the polymerization. At 480 °C, a small weight loss of 4 % was observed due to the collapse of MOF within the grafted sample. cPIM-1 showed two stages of significant weight loss due to carboxylic acid group and polymer backbone decomposition. Crosslinked cPIM-1 (20 mol%) showed three significant weight losses. The samples showed an initial loss of weight similar to that of MOF-74, but no major weight loss until around 420 °C, possibly attributed to MOF-74 structure collapse. Initial weight losses in crosslinked MMMs may be attributed to evaporation of volatile compounds, moisture and DMF trapped in MOF-74 structures, similar to neat MOF-74. Crosslinked cPIM-1 (3 mol%) showed only two major weight losses, as expected for a lower amount of MOF-74.

FT-IR spectra of PIM-1, cPIM-1, MOF-74 and grafted and crosslinked self-standing MMMs are presented in Fig. 5. Changes in intensity of –OH absorption in MOF-74 can be attributed to the MOF, water, and methanol. Upon grafting, a slight increase in –OH absorption is observed for both grafted samples. Magnified FT-IR spectra showing changes in –OH stretching are included in Fig. S24. However, both grafted PIM-1/Ni- and Co-MOF-74 did not produce significant shifts or changes, possibly due to overlapping peaks, low amount of MOF compared to polymer phase and possible losses of MOF-74 during purification of the polymer.

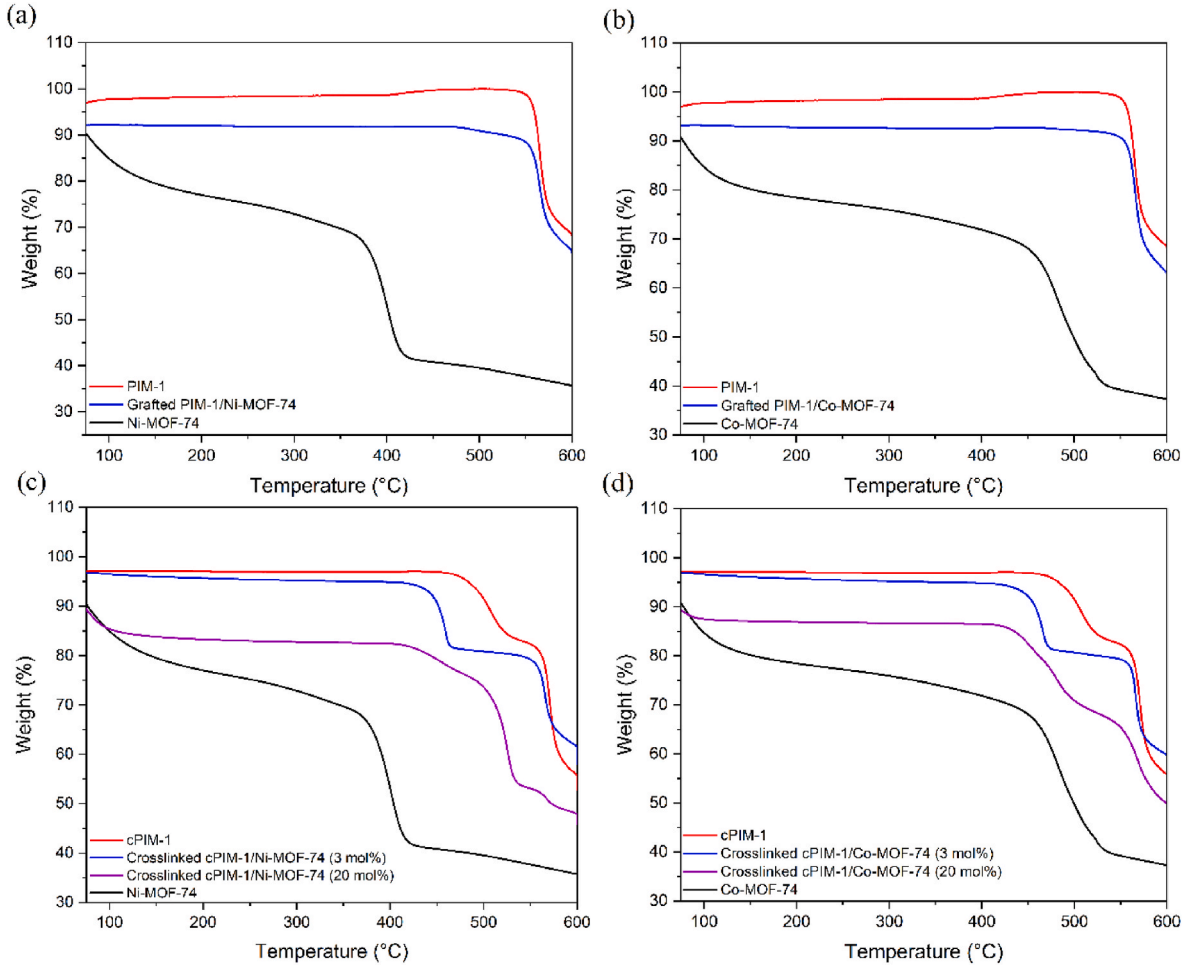

Fig. 4. TGA analysis of (a) PIM-1, Ni-MOF-74 and grafted PIM-1/Ni-MOF-74 (10 %), (b) PIM-1, Co-MOF-74 and grafted PIM-1/Co-MOF-74 (10 %), (c) cPIM-1, Ni-MOF-74, crosslinked cPIM-1/Ni-MOF-74 (3 mol%) and crosslinked cPIM-1/Ni-MOF-74 (20 mol%), (d) cPIM-1, Co-MOF-74, crosslinked cPIM-1/Co-MOF-74 (3 mol%) and crosslinked cPIM-1/Co-MOF-74 (20 mol%).

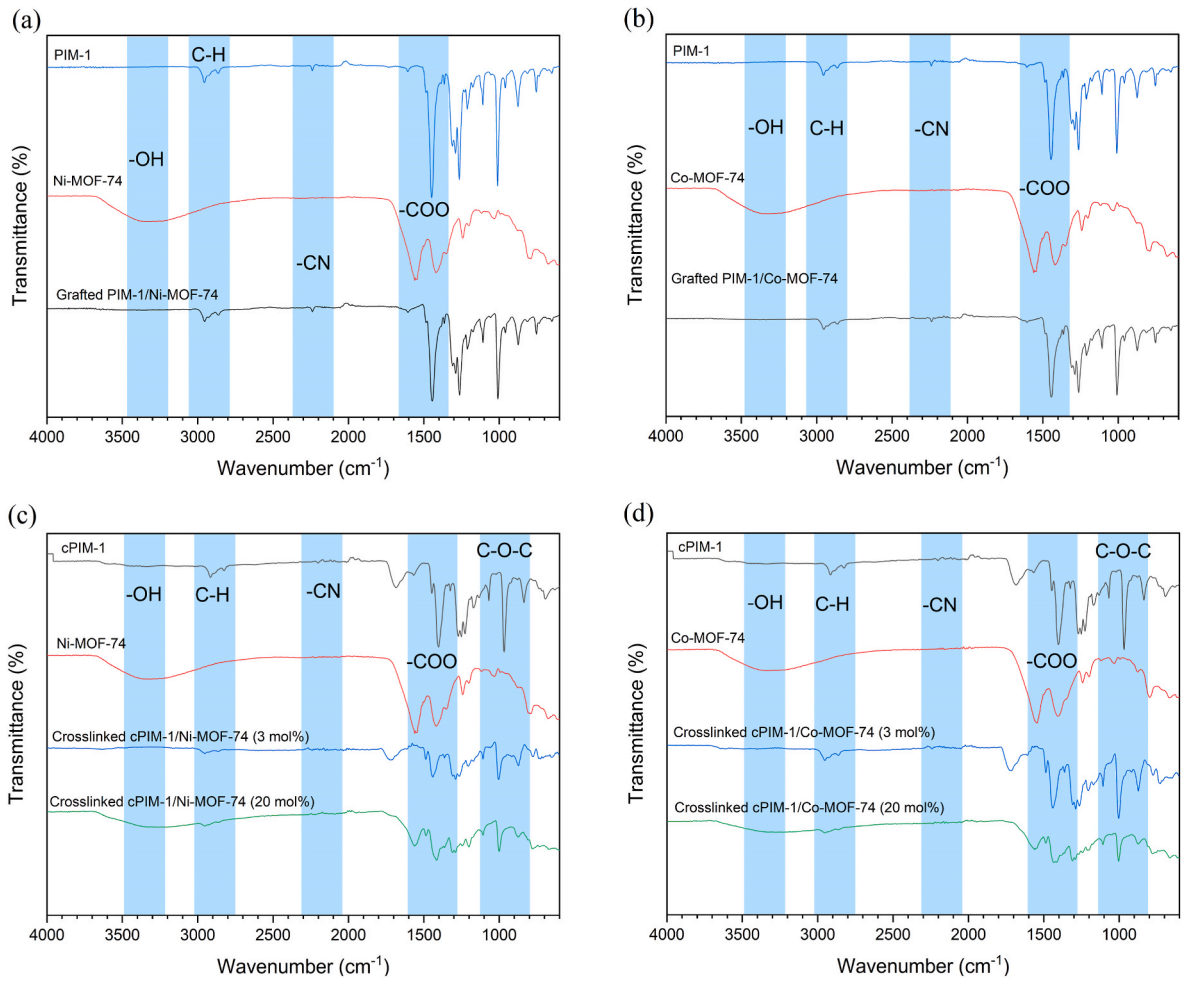

Fig. 5. FT-IR spectra of (a) PIM-1, Ni-MOF-74 and grafted PIM-1/Ni-MOF-74 (10 %), (b) PIM-1, Co-MOF-74 and grafted PIM-1/Co-MOF-74 (10 %), (c) cPIM-1, Ni-MOF-74, crosslinked cPIM-1/Ni-MOF-74 (3 mol%) and crosslinked cPIM-1/Ni-MOF-74 (20 mol%), (d) cPIM-1, Co-MOF-74, crosslinked cPIM-1/Co-MOF-74 (3 mol%) and crosslinked cPIM-1/Co-MOF-74 (20 mol%).

FT-IR spectra of crosslinking between cPIM-1 and M-MOF-74 (M = Ni or Co) are presented in Fig. 5c and d. FT-IR was carried out on crosslinked samples at two different crosslinking degrees to show differences. There is a clear difference between cPIM-1 and crosslinked cPIM-1/M-MOF-74 (3 mol%). However, the difference is small due to the small content of MOF-74 in the sample. On the other hand, crosslinked cPIM-1/M-MOF-74 (20 mol%) shows a significant increase in transmittance in the –OH stretch, attributed to the presence of MOF phase. Another observation is that the carboxylic acid (−C═O) stretch at 1710 cm^{-1} decreases upon crosslinking of cPIM-1. Changes in the alkyl groups at 2950 cm^{-1} ($–CH_3$, $–CH_2–$) of cPIM-1 are also observed. This suggests that crosslinking between the cPIM-1 and M-MOF-74 has occurred.

SEM of PIM-1 and cPIM-1 powder, cPIM-1, in-situ crosslinked cPIM-1/Ni-MOF-74 and Co-MOF-74 self-standing MMMs at different mol% concentration are included in the SI, Figs. S25–S30. The membranes were washed a few times with methanol and THF to make sure that any unattached MOF was removed before SEM analysis. Clear differences can be seen between cPIM-1 and crosslinked Ni-based samples, where Ni-MOF-74 nanoparticles can be seen on top of the crosslinked cPIM-1 membrane (Fig. S27). Ni-MOF-74 seems to create big agglomerates on the surface from fused smaller nanoparticles. Fig. S28 shows the cross-section of crosslinked cPIM-1-25%/Co-MOF-74 (8 mol% per carboxylic acid group in polymer). Co-MOF-74 nanoparticles can also be seen in the cross-section and seem to be dispersed well across the membrane, but with different morphology to that on the surface. EDS of cPIM-1/Ni- and Co-MOF-74 (8 mol%) self-standing membrane are presented in Figs. S31 and S32, respectively.

For TFN membranes, surface and cross-sectional analysis by SEM for a crosslinked cPIM-1/Ni-MOF-74 (3 mol%) TFN membrane are presented in Fig. 6. For surface analysis, EDS mapping of Ni confirms an even distribution across the TFN membrane surface. The selective layer is highlighted with a red box in Fig. 6c. EDS mapping also confirmed the Ni to be evenly distributed across the cross-section. cPIM-1/Co-MOF-74 (3 mol%) TFN membrane SEM and EDS analysis is shown in Fig. 7. The Co was confirmed to be evenly distributed across the selective layer. Fig. 7c shows cross-sectional SEM images of the fabricated TFN membranes for mixed permeation testing. SEM images suggest that the selective layer is between 1.1 μm–2.2 μm in thickness with no evidence of penetration of the polymer into the PAN layer. Additional SEM images of B-cPIM-1/M-MOF-74 (3 mol%) TFN are included in Fig. S33. Figs. S34 and S35 present cross-sectional TEM analysis of blended, grafted and crosslinked TFN membranes, along with respective EDS analysis to show the dispersion of MOF NPs. Grafted TFN showed better overall dispersion compared to blended samples, which can be seen in TEM images for Ni-MOF-74-based TFN in Figs. S34a and S34b. Notably, Fig. S36 highlights the difference between blending and grafting in PIM-1 with Co-MOF-74 samples, where there is clearer contrast between irregular aggregated nanoparticles in the cross-section of the TFN blended samples compared to more even distribution of nanoparticles in the grafted TFN sample.

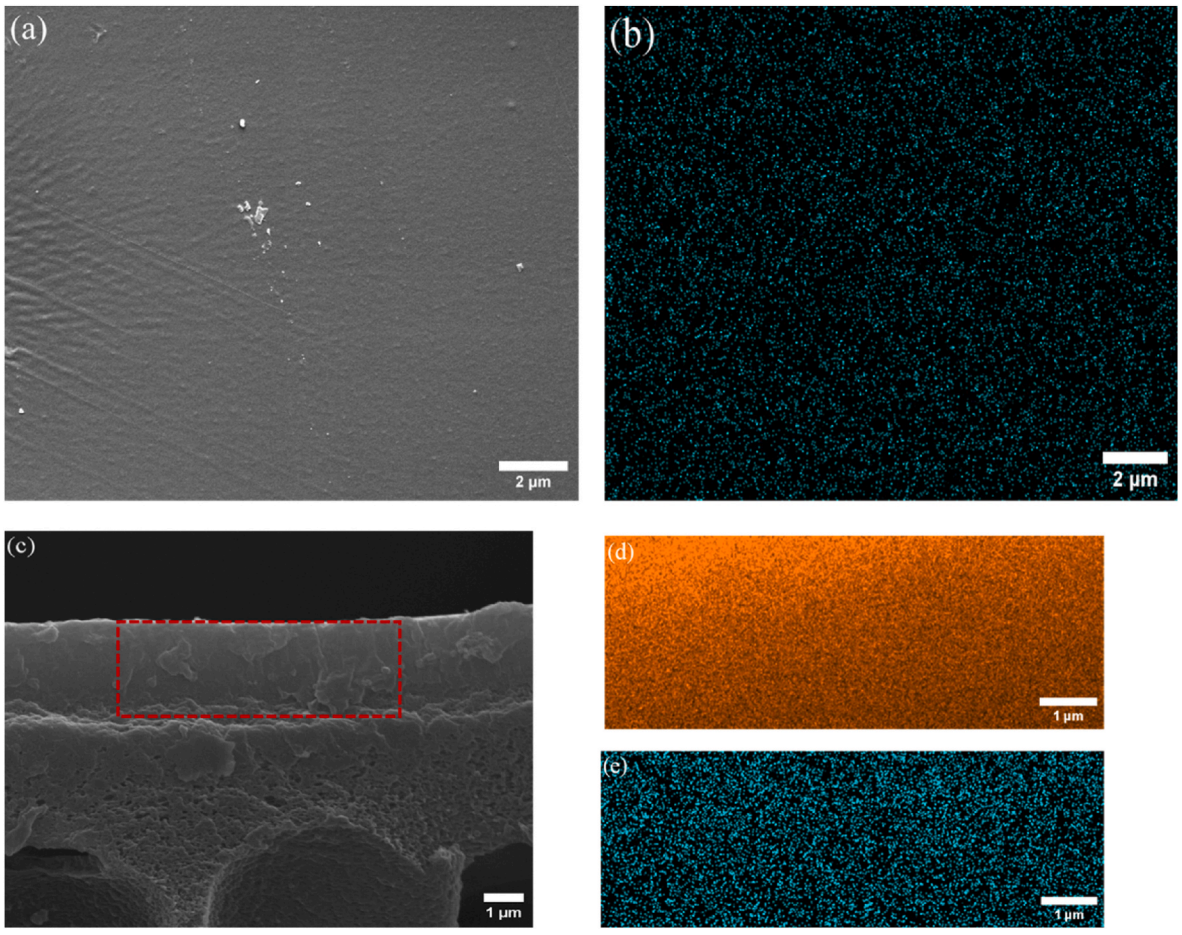

Fig. 6. SEM of crosslinked cPIM-1/Ni-MOF-74 (3 mol%) TFN showing (a) surface of TFN membrane, (b) EDS mapping of Ni, (c) cross-section of TFN membrane (red rectangle indicates area of selective layer mapped in (d) and (e), (d) cross-section EDS mapping of C, and (e) cross-section EDS mapping of Ni. (For interpretation of the references to color in this figure legend, the reader is referred to the Web version of this article.)

3.4. Single gas permeability of self-standing mixed matrix membranes

The CO_2, N_2 and CH_4 permeation data for all fabricated self-standing membranes are included in Table S5 with aging data from day 1 to day 30. The majority of the fabricated self-standing MMMs were highly brittle and difficult to cut to a suitable size for the permeation cell. This was clearly seen with aged membranes as well as with cPIM-1 samples with high hydrolysis degree. cPIM-1b with low conversion (25 %) was used to minimize the brittleness of the MMMs in crosslinked samples. PIM-1-based grafted samples were more durable and easier to test in comparison, which was attributed to a more even dispersion of MOF-74 NPs. The CO_2/N_2 data are shown in a Robeson plot in Fig. 8 for PIM-1-based and cPIM-1-based samples. Initial testing of PIM-1a samples has shown comparable results to those obtained in literature [11,51]. with a permeability of 7600 Barrer and a selectivity of 12.1. Physical blends of PIM-1a polymers with Ni-MOF-74 showed an improvement in permeability for PIM-1/Ni-MOF-74 (5 %), with CO_2 permeability of more than 10,000 Barrer, while also maintaining selectivity. Although Ni-based MMMs maintained higher permeability values after 30 days of aging, nonetheless a 30 % decrease in Ni MMMs was observed from 10,000 to 7000 Barrer, compared to only 13 % decrease in CO_2 permeability in pristine PIM-1. MMMs of PIM-1/Co-MOF-74 were difficult to test due to brittleness of the membranes.

In grafted samples, gas permeation results showed enhanced permeability for Ni samples, with slight improvement in selectivity from 12.1 to 13.3. Grafted Co-based MMMs produced similar permeability, but with enhanced selectivity from 12.1 to 15.2. However, grafted MMMs aged faster compared to pristine PIM-1 samples. It is worth noting that CO_2/CH_4 selectivities for both grafted Ni- and Co-based MMMs were noticeably higher for fresh and aged membranes compared to neat PIM-1 samples. The CO_2/N_2 and CO_2/CH_4 gas separation performances for cPIM-1b (25 %) showed reduction in CO_2 permeability associated with a significant increase in selectivity, compared to PIM-1.

Crosslinked cPIM-1/Ni-MOF-74 MMMs showed a slight increase in permeability with significantly lower selectivity. However, upon aging, the selectivity increased to 22.3 (similar level to neat cPIM-1-25 %) and permeability was maintained, which is not the case with cPIM-1-25%, whose permeability decreased by 27 %. On the other hand, membranes of crosslinked cPIM-1 with Co-MOF-74 produced significantly improved gas permeability and CO_2/N_2 and CO_2/CH_4 ideal selectivity compared to neat cPIM-1-25%, exceeding the 2008 Robeson upper bound. Based on that, efforts were made to increase the content of Co-MOF-74 from 8 mol% to 16 mol% per carboxylic acid unit in cPIM-1-25%. The self-standing membranes produced were even more brittle compared to highly hydrolyzed cPIM-1 samples (cPIM-1-60%). The gas permeation results produced higher permeability than neat cPIM-1, and significant improvement in selectivity from 17.1 in cPIM-1-25% to 47 in crosslinked cPIM-1-25%/Co-MOF-74 (16 mol%), exceeding current 2019 Robeson upper bounds. Aged samples showed a slight drop in permeability associated with boost in selectivity in both CO_2/N_2 and CO_2/CH_4. Further testing of aging was not possible due to the brittleness of these crosslinked self-standing membranes.

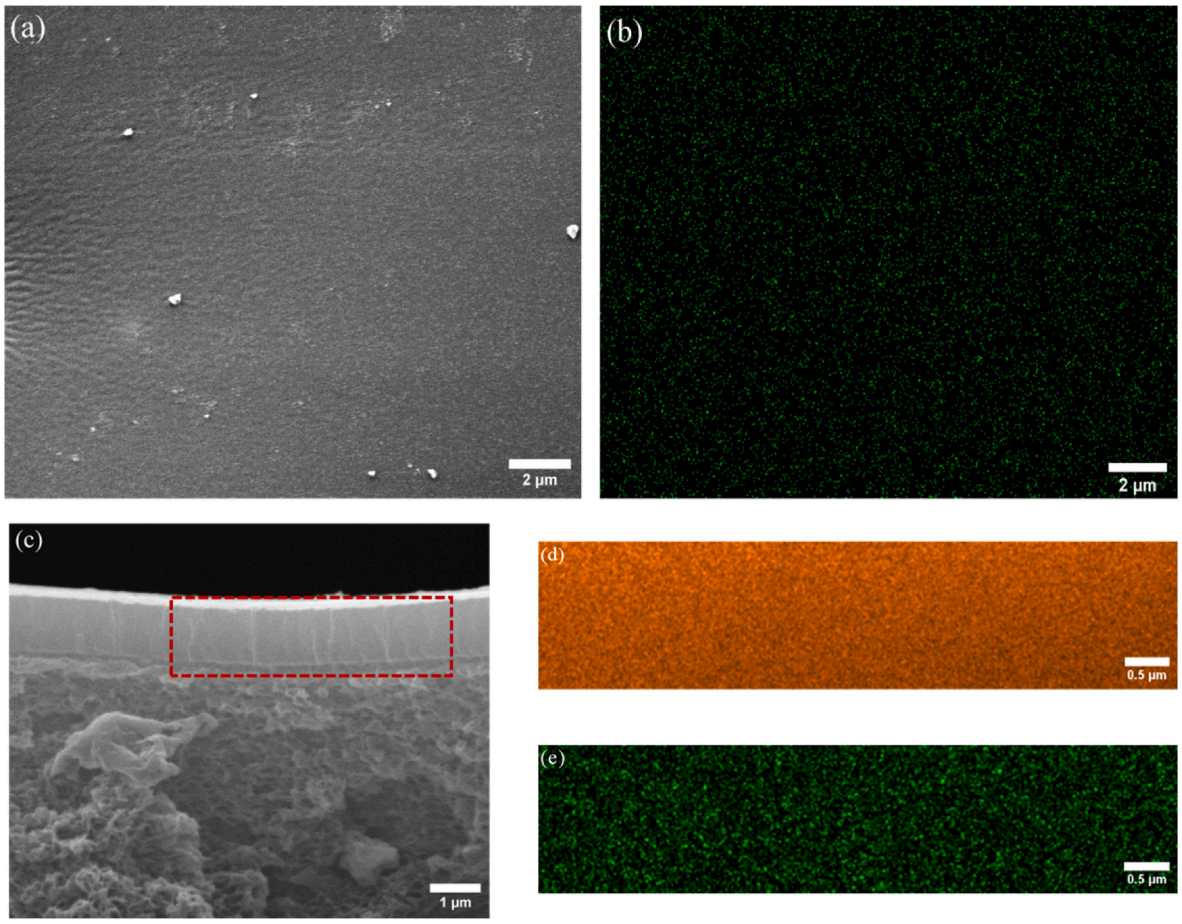

Fig. 7. SEM of crosslinked cPIM-1/Co-MOF-74 (3 mol%) TFN showing (a) surface of TFN membrane, (b) EDS mapping of Co, (c) cross-section of TFN membrane (red rectangle indicates area of selective layer mapped in (d) and (e), (d) cross-section EDS mapping of C, and (e) cross-section EDS mapping of Co.

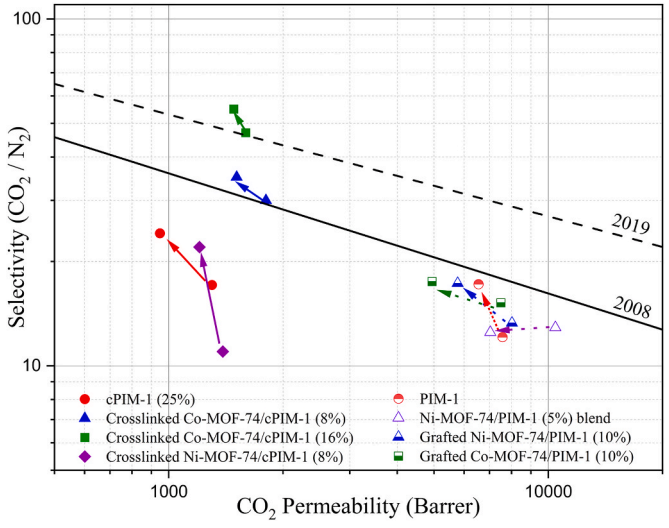

Fig. 8. Plot of ideal CO_2/N_2 selectivity vs. CO_2 permeability, with Robeson [52] 2008 and Jansen/McKeown [53] 2019 upper bounds, showing data on day 1 and day 30 for self-standing films prepared from pristine PIM-1, PIM-1/Ni-MOF-74 (5 %) blend, grafted PIM-1/Ni-MOF-74 (10 %), grafted PIM-1/Co-MOF-74 (10 %), hydrolyzed PIM-1 (25 %), crosslinked Co-MOF-74/cPIM-1 (8 % by mol per carboxylic acid group) and crosslinked Co-MOF-74/cPIM-1 (16 % by mol). The arrows indicate membrane aging trends from day 1 to day 30.

3.5. Single gas permeance of thin film composite and thin film nanocomposite membranes

The CO_2, N_2 and CH_4 permeation data for all fabricated TFC and TFN membranes are included in Table S6 with aging from day 1 to day 28. Initial studies on TFN membranes prepared from PIM-1a and M-MOF-74 (M = Ni or Co) using conventional physical blending were done on Sepro PA350 and SolSep UF support materials (Fig. 9a and b). These TFN membranes were prepared from 3 % w/v PIM-1 with 5 % w/w of Ni- or Co-MOF-74 nanoparticles. PIM-1/Ni- and Co-MOF-74 (5 %) TFN membranes showed significant increases in permeance, with 152 % and 112 % increase for Ni-based and Co-based TFNs, respectively, compared to neat PIM-1 TFC membranes. However, no significant changes in CO_2/N_2 selectivity were observed by blending Ni- and Co-MOF-74 in this manner. These results may suggest the formation of interfacial voids between the polymer and MOF matrices. In addition, physical aging showed a slightly faster aging rate, 88 % permeance decrease for Ni-based samples, compared with 82 % permeance decrease for PIM-1 TFC membranes. On the other hand, aged TFN membranes of Ni- and Co-MOF-74 showed higher permeance with similar selectivity compared to PIM-1 TFC membrane at the same time of aging. A noticeable difference in the separation performance was observed upon the change of support from Sepro PA350 to SolSep UF, both composed of polyacrylonitrile. Slightly lower permeance and selectivity with faster physical aging for TFNs of PIM-1 with Ni- and Co-MOF-74 was generally observed when using the SolSep support. This might be due to the pore size in UF 010104-1501 (55 nm), which is slightly larger than in PA350 (35 nm), which allowed penetration of polymer solution into the support, leading to reduction in permeance. Another factor is the impact of

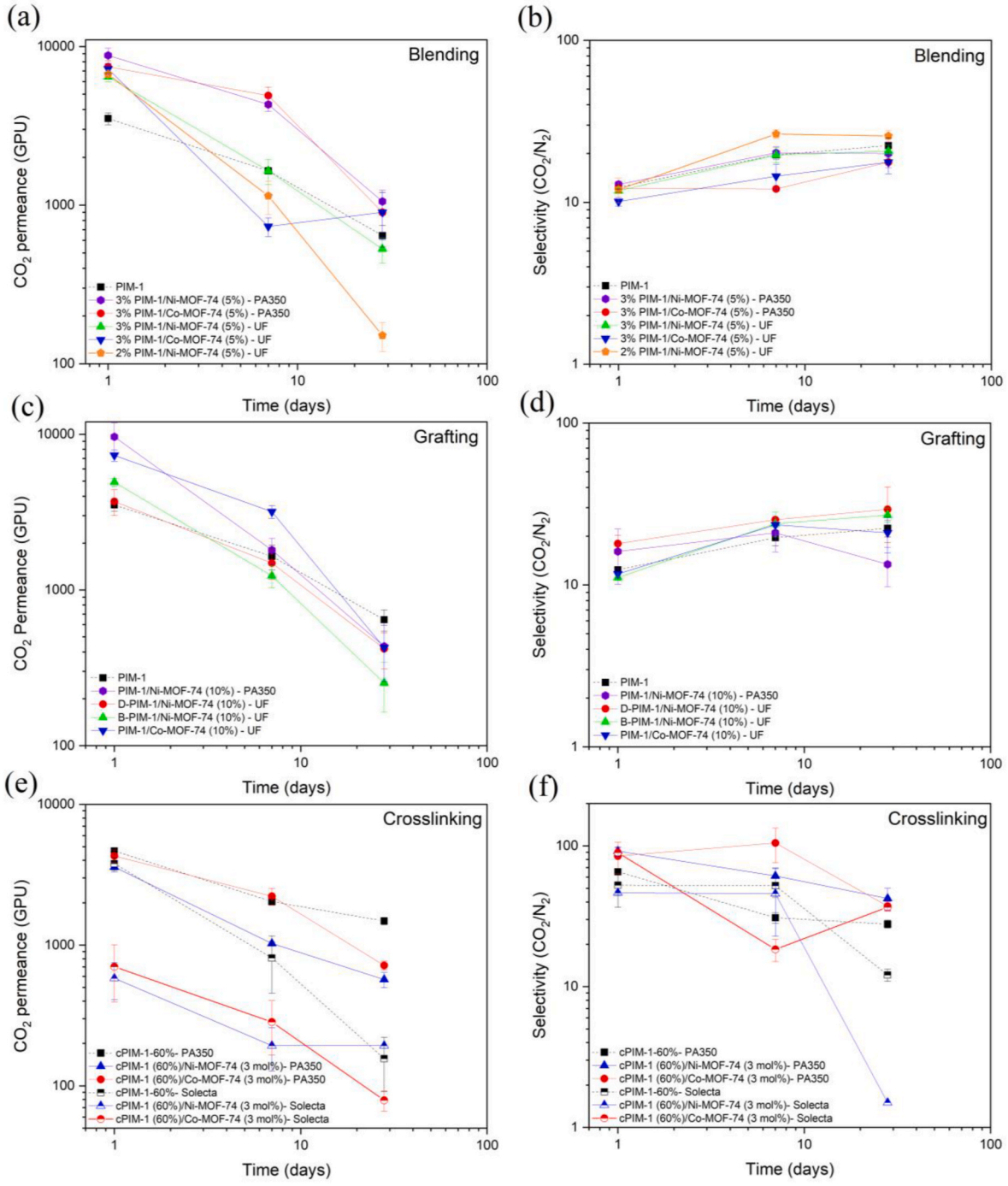

Fig. 9. Dependence on aging time of gas permeation data for TFCs and TFNs on Sepro PA350, SolSep UF and Solecta supports showing (a) CO_2 permeance for samples prepared via conventional blending between 3 % w/v PIM-1 and MOF-74 (5 % w/w), (b) ideal CO_2/N_2 selectivity for conventional blending 3 % w/v PIM-1 and MOF-74 (5 % w/w), (c) CO_2 permeance for samples prepared via 3 % w/v PIM-1 and grafting with MOF-74 (10 % w/w), (d) ideal CO_2/N_2 selectivity for samples prepared via 3 % w/v PIM-1 and grafting with MOF-74 (10 % w/w), (e) CO_2 permeance for samples prepared via 4 % w/v cPIM-1 and MOF-74 (3 mol%) in-situ crosslinking and (f) ideal CO_2/N_2 selectivity for samples prepared via 4 % w/v cPIM-1 and MOF-74 (3 mol%) in-situ crosslinking.

casting solvent on the porosity of the UF 010104 support compared to PA350, as shown previously by Yu et al. [11].

Results for TFN membranes with grafted fillers are shown in Fig. 9c and d. Grafted PIM-1/Ni-MOF-74 on PA350 produced significant initial permeance improvement to 9600 GPU, highest across all fabricated TFN membranes, with improved CO_2/N_2 selectivity from 12 to 16, compared to a neat PIM-1 sample. However, a significant drop in permeance and selectivity was observed after 28 days of aging. With UF 010104-1501 support, reduced initial permeance was noted compared to PA350. However, slower aging was observed with higher selectivity, with similar trend to self-standing MMMs.

cPIM-1b-60% and crosslinked cPIM-1b/M-MOF-74 samples are shown in Fig. 9e and **f** cPIM-1-60% coated on PA350 showed high ideal selectivity (66 for CO_2/N_2) and comparable permeance to that of PIM-1. However, a drop in aged cPIM-1b-60% permeance and selectivity was observed after 28 days; similar results for this hydrolysis conversion range were previously reported by Yu et al. [11]. Crosslinked cPIM-1b-60%/M-MOF-74 (3 mol%) showed significantly increased ideal

CO_2/N_2 selectivities of 92 and 85 for Ni and Co-based samples, respectively. Similar behavior was also observed for ideal CO_2/CH_4 selectivity, which increased from 36 to 50. Aging behavior was similar to that of neat cPIM-1-60%, which could indicate that M-MOF-74 can boost gas separation performance significantly, but aging will solely depend on the polymer phase. Therefore, cPIM-1 with higher conversion might help to retain performance on aging, while benefiting from the MOF-74 in enhancing permeance and selectivity. Another set of experiments was carried out on a different support (Solecta) to study how it would affect the performance compared to PA350. The results show a significant drop in permeance and selectivity for both neat cPIM-1 and crosslinked MMMs, which indicates that choice of support plays a significant role in thin film fabrication. Although Solecta support has been shown in our laboratory to perform well with PIM-1 samples, it didn't work so well with cPIM-1. This might be because of possible interaction between the support and polymeric materials on the surface of the support. Another possibility is the change of solvent from chloroform to THF partially deforming and blocking the finger-like pores in the PAN support, leading to reduced permeance and selectivity. The performance of TFN membranes for CO_2/CH_4 are included in the SI (Fig. S37).

Fig. 10 Summarizes ideal CO_2/N_2 selectivity vs CO_2 permeance of all fabricated TFN membranes on PA350 support, compared to the industrially favorable region for post-combustion carbon capture, introduced by Merkel et al. [28]. Ideal gas separation performance for some of the fabricated TFN membranes fall in the targeted region. The introduction of M-MOF-74 gives a significant increase in permeance in all PIM-1 based samples, with slight positive change in selectivity, especially for grafted B-PIM-1a/Ni-MOF-74 (10 %). cPIM-1 based TFN membranes are shown to maintain permeance with significant increase in ideal selectivity for fresh membranes, which is still higher than cPIM-1 after aging. Ideal gas selectivities may differ significantly from mixed gas results due to plasticization, as seen with cPIM-1 TFC membranes [11]. However, research has shown that addition of fillers like MOFs could limit the movement of polymers chains thus overcoming CO_2 plasticization [54].

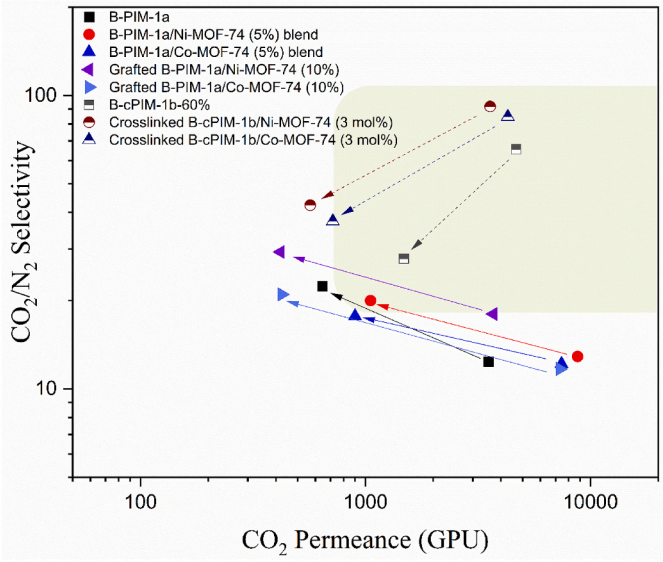

Fig. 10. Plot of ideal CO_2/N_2 selectivity vs. CO_2 permeance showing performance of TFN membranes prepared from PIM-1 and cPIM-1 by conventional blending, in-situ grafting and crosslinking, compared against the favored range for post-combustion carbon capture suggested by Merkel et al. [28] (shaded region). All samples were coated on Sepro PA350 support apart from grafted PIM-1/Ni-MOF-74 and Co-MOF-74, which were coated on SolSep UF 010104-1501 support. Arrows indicate physical aging of TFN membranes from day 1 to day 28. Solid lines are for PIM-1 based samples, while dashed lines are for cPIM-1 based samples.

Table 2
Mixed gas separation performance of TFC membranes on PA350 support of B-cPIM-1, crosslinked B-cPIM-1/Ni-MOF-74 (3 mol%) and crosslinked B-cPIM-1/Co-MOF-74 (3 mol%) from 50 %/50 % CO_2/N_2 feed.

Membrane Configuration		Permeance and Selectivity			
Selective layer	Thickness (μm)	Aging (days)	N_2 (GPU)	CO_2 (GPU)	CO_2/N_2
B-cPIM-1c	1.1	1	49 ± 31	1014 ± 287	24 ± 9
		38	21 ± 14	387 ± 70	23 ± 12
Crosslinked cPIM-1c/Ni-MOF-74 3 mol%)	1.8	1	31 ± 10	982 ± 191	32 ± 5
		38	22 ± 7	598 ± 49	30 ± 8
Crosslinked cPIM-1c/Co-MOF-74 3 mol%)	2.2	1	59 ± 10	1842 ± 668	33 ± 7
		38	24 ± 6	525 ± 91	23 ± 2

3.6. Mixed gas permeance of thin film composite and thin film nanocomposite membranes

cPIM-1, like other glassy polymers, is susceptible to plasticization effects by highly sorbing gases such as CO_2, leading to reduced selectivity. Recent work by Yu et al. [11] showed that cPIM-1 under mixed gas conditions (90 % N_2/10 % CO_2) produced lower permeance (700–1000 GPU) and lower CO_2/N_2 selectivity (13–19) compared to ideal gas separation performance (1000–1900 GPU and CO_2/N_2 of 36–86). TFNs of cPIM-1c, and cPIM-1c crosslinked with Ni- and Co-MOF-74 were assessed using a mixed gas separation system measuring CO_2/N_2 and CO_2/CH_4 selectivities from a 50 %/50 % feed composition. Table 2 summarizes the results obtained for CO_2/N_2 mixture for fresh and aged membranes. Permeance and selectivity were both reduced compared to ideal gas conditions. cPIM-1 TFC produced a permeance of 1014 GPU and a CO_2/N_2 selectivity of 25. Crosslinked cPIM-1/Ni-MOF-74 TFNs showed similar permeance and higher selectivity than the parent cPIM-1. Overall, these crosslinked cPIM-1/Ni-MOF-74 TFNs produced the highest permeance and selectivity upon aging in mixed gas conditions, compared to neat cPIM-1 and Co-based TFN, which may indicate some plasticization resistance upon crosslinking. The performance of aged TFN membranes were also tested with a CO_2/CH_4 mixture with 50 %/50 % composition and results are included in the SI (Table S7).

4. Conclusions

Multiple fabrication routes to produce mixed matrix and TFN membranes were investigated to enhance interfacial interaction, optimize membrane performance, and mitigate aging and plasticization effects. Conventional blending of PIM-1 samples with M-MOF-74 (M = Ni or Co) gave TFN membranes with improved gas separation performance compared to neat PIM-1 TFC membranes. An aged TFN membrane of PIM-1 blended with Ni-MOF-74 showed a permeance of 1000 GPU and selectivities of 20.0 and 20.5 for CO_2/N_2 and CO_2/CH_4, respectively.

Grafting enhanced the interfacial interaction between the two matrices to give more durable self-standing films. A fresh TFN membrane of grafted PIM-1/Ni-MOF-74 gave high permeance, reaching 9600 GPU with CO_2/N_2 ideal selectivity of 16.

Crosslinking showed significantly improved permeability and selectivity, exceeding the current 2019 upper bound for pure gas permeation in self-standing membranes of cPIM-1 crosslinked with Co-MOF-74. On PA350 support, crosslinked cPIM-1 TFN membranes showed significant increase in ideal selectivity, increasing from 66 to 92 and 85 CO_2/N_2 for Ni- and Co-based MOFs, respectively. In this study, selection of support materials proved to be significant for gas separation performance, especially long-term physical aging. Mixed gas performance on Ni and Co-based crosslinked samples produced CO_2 permeances of 980 GPU

and 1840 GPU, respectively, and CO_2/N_2 selectivities of 32 and 33, respectively. Further studies of support interactions with these polymers need to be conducted to obtain maximum performance and improve resistance to physical aging and plasticization effects.

CRediT authorship contribution statement

Mustafa Alshurafa: Writing – original draft, Methodology, Formal analysis. **Andrew B. Foster:** Writing – review & editing, Supervision. **Sulaiman Aloraini:** Investigation. **Ming Yu:** Investigation. **Boya Qiu:** Investigation, Writing – review & editing. **Patricia Gorgojo:** Supervision, Writing – review & editing. **Martin P. Attfield:** Writing – review & editing, Supervision. **Peter M. Budd:** Writing – review & editing, Supervision, Project administration, Funding acquisition.

Declaration of competing interest

The authors declare that they have no known competing financial interests or personal relationships that could have appeared to influence the work reported in this paper.

Data availability

Data supporting this study are available within the Article and the Supplementary Information.

Acknowledgements

MA acknowledges the Department of Research & Analytical services, Saudi Aramco, for PhD sponsorship. ABF acknowledges the support of the Engineering and Physical Sciences Research Council (EPSRC) grant EP/V047078/1 (SynHiSel). SA is sponsored by Qassim University, Saudi Arabia. MY is grateful to the University of Melbourne for a Melbourne Research scholarship for a dual award PhD programme between the University of Melbourne and the University of Manchester. BQ would like to thank the China Scholarship Council (CSC, file no. 202006240076) and the University of Manchester for the joint PhD studentship to support her PhD research. We are grateful to Anne Davies and Martin Jennings for their assistance in obtaining the elemental analysis and TGA.

Appendix A. Supplementary data

Supplementary data to this article can be found online at https://doi.org/10.1016/j.memsci.2024.123388.

References

[1] M. Liu, K. Xie, M.D. Nothling, P.A. Gurr, S.S.L. Tan, Q. Fu, P.A. Webley, G.G. Qiao, Ultrathin metal-organic framework nanosheets as a gutter layer for flexible composite gas separation membranes, ACS Nano 12 (2018) 11591–11599, https://doi.org/10.1021/acsnano.8b06811.

[2] O. Edenhofer, R. Pichs-Madruga, Y. Sokona, E. Farahani, S. Kadner, K. Seyboth, A. Adler, I. Baum, S. Brunner, P. Eickemeier, B. Kriemann, J. Savolainen, S. Schlömer, C. von Stechow, T. Zwickel and J.C. Minx, Climate Change 2014: Mitigation of Climate Change, Cambridge University Press, Cambridge, United Kingdom and New York, NY, USA. https://www.ipcc.ch/site/assets/uploads/2018/02/ipcc_wg3_ar5_full.pdf (accessed 2022-December-10).

[3] Environmental Protection Agency, US, Inventory of U.S. Greenhouse gas emissions and sinks: 1990-2019. https://www.epa.gov/ghgemissions/inventory-us-greenhouse-gas-emissions-and-sinks-1990-2019, April, 2021. (Accessed 12 September 2022).

[4] L. Chancel, T. Piketty, E. Saez, G. Zucman, et al., World inequality report world inequality lab. https://wir2022.wid.world/www-site/uploads/2021/12/WorldInequalityReport2022_Full_Report.pdf, 2022. (Accessed 7 May 2023).

[5] K.K. Wong, Z.A. Jawad, A review and future prospect of polymer blend mixed matrix membrane for CO_2 separation, J. Polym. Res. 26 (2019), https://doi.org/10.1007/s10965-019-1978-z.

[6] C.Z. Liang, T.-S. Chung, J.-Y. Lai, A review of polymeric composite membranes for gas separation and energy production, Prog. Polym. Sci. 97 (2019) 101141, https://doi.org/10.1016/j.progpolymsci.2019.06.001.

[7] P.M. Budd, B.S. Ghanem, S. Makhseed, N.B. McKeown, K.J. Msayib, C. E. Tattershall, Polymers of intrinsic microporosity (PIMs): robust, solution-processable, organic nanoporous materials, Chem. Commun. (2004) 230–231, https://doi.org/10.1039/b311764b.

[8] P.M. Budd, E.S. Elabas, B.S. Ghanem, S. Makhseed, N.B. McKeown, K.J. Msayib, C. E. Tattershall, D. Wang, Solution-processed, organophilic membrane derived from a polymer of intrinsic microporosity, Adv. Mater. 16 (2004) 456–459, https://doi.org/10.1002/adma.200306053.

[9] S. Bandehali, A. Ebadi Amooghin, H. Sanaeepur, R. Ahmadi, A. Fuoco, J.C. Jansen, S. Shirazian, Polymers of intrinsic microporosity and thermally rearranged polymer membranes for highly efficient gas separation, Sep. Purif. Technol. 278 (2021) 119513, https://doi.org/10.1016/j.seppur.2021.119513.

[10] L.M. Robeson, Correlation of separation factor versus permeability for polymeric membranes, J. Membr. Sci. 62 (1991) 165–185, https://doi.org/10.1016/0376-7388(91)80060-j.

[11] M. Yu, A.B. Foster, M. Alshurafa, J.M. Luque-Alled, P. Gorgojo, S.E. Kentish, C. A. Scholes, P.M. Budd, CO_2 separation using thin film composite membranes of acid-hydrolyzed PIM-1, J. Membr. Sci. 679 (2023) 121697, https://doi.org/10.1016/j.memsci.2023.121697.

[12] H. Daglar, S. Aydin, S. Keskin, MOF-based MMMs breaking the upper bounds of polymers for a large variety of gas separations, Sep. Purif. Technol. 281 (2022) 119811, https://doi.org/10.1016/j.seppur.2021.119811.

[13] D. Fan, A. Ozcan, N.A. Ramsahye, G. Maurin, R. Semino, Putting forward NUS-8-CO_2 H/PIM-1 as a mixed matrix membrane for CO_2 capture, ACS Appl. Mater. Interfaces 14 (2022) 16820–16829, https://doi.org/10.1021/acsami.2c00090.

[14] F. Emamverdi, J. Huang, N.M. Razavi, M.J. Bojdys, A.B. Foster, P.M. Budd, M. Bohning, A. Schonhals, Molecular mobility and gas transport properties of mixed matrix membranes based on PIM-1 and a phosphinine containing covalent organic framework, Macromolecules 57 (2024) 1829–1845, https://doi.org/10.1021/acs.macromol.3c02419.

[15] T.H. Lee, B.K. Lee, C. Youn, J.H. Kang, Y.J. Kim, K.I. Kim, Y.R. Ha, Y. Han, H. B. Park, Interface engineering in MOF/crosslinked polyimide mixed matrix membranes for enhanced propylene/propane separation performance and plasticization resistance, J. Membr. Sci. 667 (2023) 121182, https://doi.org/10.1016/j.memsci.2022.121182.

[16] Y. Pu, Z. Yang, V. Wee, Z. Wu, Z. Jiang, D. Zhao, Amino-functionalized NUS-8 nanosheets as fillers in PIM-1 mixed matrix membranes for CO_2 separations, J. Membr. Sci. 641 (2022), https://doi.org/10.1016/j.memsci.2021.119912.

[17] O.K. Farha, I. Eryazici, N.C. Jeong, B.G. Hauser, C.E. Wilmer, A.A. Sarjeant, R. Q. Snurr, S.T. Nguyen, A.O. Yazaydin, J.T. Hupp, Metal-organic framework materials with ultrahigh surface areas: is the sky the limit? J. Am. Chem. Soc. 134 (2012) 15016–15021, https://doi.org/10.1021/ja3055639.

[18] A. Lutton-Gething, L.T. Nangkam, J.O.W. Johansson, I. Pallikara, J.M. Skelton, G.F. S. Whitehead, I. Vitorica-Yrezabal, M.P. Attfield, Breathing behaviour modification of gallium MIL-53 metal-organic frameworks induced by the bridging framework inorganic anion, Chemistry 29 (2023) e202203773, https://doi.org/10.1002/chem.202203773.

[19] L. Liu, Z. Chen, J. Wang, D. Zhang, Y. Zhu, S. Ling, K.W. Huang, Y. Belmabkhout, K. Adil, Y. Zhang, B. Slater, M. Eddaoudi, Y. Han, Imaging defects and their evolution in a metal-organic framework at sub-unit-cell resolution, Nat. Chem. 11 (2019) 622–628, https://doi.org/10.1038/s41557-019-0263-4.

[20] I. Thomas-Hillman, A. Laybourn, C. Dodds, S.W. Kingman, Realising the environmental benefits of metal–organic frameworks: recent advances in microwave synthesis, J. Mater. Chem. A 6 (2018) 11564–11581, https://doi.org/10.1039/c8ta02919a.

[21] D. Britt, H. Furukawa, B. Wang, T.G. Glover, O.M. Yaghi, Highly efficient separation of carbon dioxide by a metal-organic framework replete with open metal sites, Proc. Natl. Acad. Sci. U. S. A. 106 (2009) 20637–20640, https://doi.org/10.1073/pnas.0909718106.

[22] Y. Yang, L. Jin, L. Zhou, X. Du, A molecular study of humid CO_2 adsorption capacity by Mg-MOF-74 surfaces with ligand functionalization, Comput. Mater. Sci. 209 (2022) 111407, https://doi.org/10.1016/j.commatsci.2022.111407.

[23] S. Gautam, D. Cole, CO_2 adsorption in metal-organic framework Mg-MOF-74: effects of inter-crystalline space, Nanomaterials 10 (2020) 2274, https://doi.org/10.3390/nano10112274.

[24] M. Díaz-García, Á. Mayoral, I. Díaz, M. Sánchez-Sánchez, Nanoscaled M-MOF-74 materials prepared at room temperature, Cryst. Growth Des. 14 (2014) 2479–2487, https://doi.org/10.1021/cg500190h.

[25] R. Selyanchyn, S. Fujikawa, Membrane thinning for efficient CO_2 capture, Sci. Technol. Adv. Mater. 18 (2017) 816–827, https://doi.org/10.1080/14686996.2017.1386531.

[26] B.A. Al-Maythalony, Metal-organic framework based membranes for gas separation, in: W.-J. Lau, A.F. Ismail, A. Isloor, A. Al-Ahmed (Eds.), Advanced Nanomaterials for Membrane Synthesis and its Applications, Elsevier, 2019, pp. 203–226, https://doi.org/10.1016/b978-0-12-814503-6.00009-4.

[27] M. Tamaddondar, A.B. Foster, M. Carta, P. Gorgojo, N.B. McKeown, P.M. Budd, Mitigation of physical aging with mixed matrix membranes based on cross-linked PIM-1 fillers and PIM-1, ACS Appl. Mater. Interfaces 12 (2020) 46756–46766, https://doi.org/10.1021/acsami.0c13838.

[28] T.C. Merkel, H. Lin, X. Wei, R. Baker, Power plant post-combustion carbon dioxide capture: an opportunity for membranes, J. Membr. Sci. 359 (2010) 126–139, https://doi.org/10.1016/j.memsci.2009.10.041.

[29] R. Lin, B. Villacorta Hernandez, L. Ge, Z. Zhu, Metal organic framework based mixed matrix membranes: an overview on filler/polymer interfaces, J. Mater. Chem. A 6 (2018) 293–312, https://doi.org/10.1039/c7ta07294e.

[30] A.M. Thomas, J. de Grooth, J.A. Wood, Synthetic guidelines for highly selective mixed matrix membranes, J. Membr. Sci. 649 (2022) 120311, https://doi.org/10.1016/j.memsci.2022.120311.
[31] C. Ma, M. Wang, Z. Wang, M. Gao, J. Wang, Recent progress on thin film composite membranes for CO_2 separation, J. CO_2 Util. 42 (2020) 101296, https://doi.org/10.1016/j.jcou.2020.101296.
[32] C.Z. Liang, W.F. Yong, T.-S. Chung, High-performance composite hollow fiber membrane for flue gas and air separations, J. Membr. Sci. 541 (2017) 367–377, https://doi.org/10.1016/j.memsci.2017.07.014.
[33] M. Liu, M.D. Nothling, P.A. Webley, J. Jin, Q. Fu, G.G. Qiao, High-throughput CO_2 capture using PIM-1@MOF based thin film composite membranes, Chem. Eng. J. 396 (2020) 125328, https://doi.org/10.1016/j.cej.2020.125328.
[34] Y. Jia, P. Liu, Y. Liu, D. Zhang, Y. Ning, C. Xu, Y. Zhang, In-situ interfacial crosslinking of NH_2-MIL-53 and polyimide in MOF-incorporated mixed matrix membranes for efficient H_2 purification, Fuel 339 (2023) 126938, https://doi.org/10.1016/j.fuel.2022.126938.
[35] W.N. Wu, K. Mizrahi Rodriguez, N. Roy, J.J. Teesdale, G. Han, A. Liu, Z.P. Smith, Engineering the polymer-MOF interface in microporous composites to address complex mixture separations, ACS Appl. Mater. Interfaces (2023), https://doi.org/10.1021/acsami.3c11300.
[36] A. Baniani, M.P. Rivera, J. Marreiros, R.P. Lively, S. Vasenkov, Influence of polymer modification on intra-MOF self-diffusion in MOF-based mixed matrix membranes, Microporous Mesoporous Mater. 359 (2023) 112648, https://doi.org/10.1016/j.micromeso.2023.112648.
[37] T.H. Lee, B.K. Lee, S.Y. Yoo, H. Lee, W.N. Wu, Z.P. Smith, H.B. Park, PolyMOF nanoparticles constructed from intrinsically microporous polymer ligand towards scalable composite membranes for CO_2 separation, Nat. Commun. 14 (2023) 8330, https://doi.org/10.1038/s41467-023-44027-y.
[38] A. Bhattacharya, Grafting: a versatile means to modify polymersTechniques, factors and applications, Prog. Polym. Sci. 29 (2004) 767–814, https://doi.org/10.1016/j.progpolymsci.2004.05.002.
[39] N. Du, G.P. Robertson, J. Song, I. Pinnau, S. Thomas, M.D. Guiver, Polymers of intrinsic microporosity containing trifluoromethyl and phenylsulfone groups as materials for membrane gas separation, Macromolecules 41 (2008) 9656–9662, https://doi.org/10.1021/ma801858d.
[40] A.B. Foster, M. Tamaddondar, J.M. Luque-Alled, W.J. Harrison, Z. Li, P. Gorgojo, P. M. Budd, Understanding the topology of the polymer of intrinsic microporosity PIM-1: cyclics, tadpoles, and network structures and their impact on membrane performance, Macromolecules 53 (2020) 569–583, https://doi.org/10.1021/acs.macromol.9b02185.
[41] S. Aloraini, M. Mathias, J. Crone, K. Bryce, M. Yu, R.A. Kirk, M.Z. Ahmad, E. D. Asuquo, S. Rico-Martinez, A.V. Volkov, A.B. Foster, P.M. Budd, Crosslinking of branched PIM-1 and PIM-Py membranes for recovery of toluene from dimethyl sulfoxide by pervaporation, ACS Appl. Polym. Mater. 5 (2023) 1145–1158, https://doi.org/10.1021/acsapm.2c01600.
[42] K. Mizrahi Rodriguez, A.X. Wu, Q. Qian, G. Han, S. Lin, F.M. Benedetti, H. Lee, W. S. Chi, C.M. Doherty, Z.P. Smith, Facile and time-efficient carboxylic acid functionalization of PIM-1: effect on molecular packing and gas separation performance, Macromolecules 53 (2020) 6220–6234, https://doi.org/10.1021/acs.macromol.0c00933.
[43] A.B. Foster, J.L. Beal, M. Tamaddondar, J.M. Luque-Alled, B. Robertson, M. Mathias, P. Gorgojo, P.M. Budd, Importance of small loops within PIM-1 topology on gas separation selectivity in thin film composite membranes, J. Mater. Chem. A 9 (2021) 21807–21823, https://doi.org/10.1039/d1ta03712a.
[44] A. Bhaskar, R. Banerjee, U. Kharul, ZIF-8@PBI-BuI composite membranes: elegant effects of PBI structural variations on gas permeation performance, J. Mater. Chem. A 2 (2014) 12962, https://doi.org/10.1039/c4ta00611a.
[45] S.C. Kumbharkar, P.B. Karadkar, U.K. Kharul, Enhancement of gas permeation properties of polybenzimidazoles by systematic structure architecture, J. Membr. Sci. 286 (2006) 161–169, https://doi.org/10.1016/j.memsci.2006.09.030.
[46] Y. Lu, C. Liu, C. Mei, J. Sun, J. Lee, Q. Wu, M.A. Hubbe, M.-C. Li, Recent advances in metal organic framework and cellulose nanomaterial composites, Coord. Chem. Rev. 461 (2022) 214496, https://doi.org/10.1016/j.ccr.2022.214496.
[47] M. Díaz-García, M. Sánchez-Sánchez, Synthesis and characterization of a new Cd-based metal-organic framework isostructural with MOF-74/CPO-27 materials, Microporous Mesoporous Mater. 190 (2014) 248–254, https://doi.org/10.1016/j.micromeso.2014.02.021.
[48] C.-N. Zhang, Y. Li, H.-L. Fan, C. Yang, M. M, A highly reversible sorption for sulfur-containing toxic VOCs emissions under ambient temperature and pressure, J. Inorg. Organomet. Polym. Mater. 30 (2019) 486–493, https://doi.org/10.1007/s10904-019-01207-y.
[49] M.Z. Ahmad, E.D. Asuquo, S. Rico-Martinez, M. Alshurafa, V. Orts-Mercadillo, A. Devarajan, A.E. Lozano, A.B. Foster, P.M. Budd, Effects of metal acetate addition on the gas separation properties of polymers of intrinsic microporosity PIM-1 and PIM-Py, Polymer 292 (2024) 126556, https://doi.org/10.1016/j.polymer.2023.126556.
[50] C.F. Holder, R.E. Schaak, Tutorial on powder X-ray diffraction for characterizing nanoscale materials, ACS Nano 13 (2019) 7359–7365, https://doi.org/10.1021/acsnano.9b05157.
[51] C.A. Scholes, S. Kanehashi, Polymer of intrinsic microporosity (PIM-1) membranes treated with supercritical CO_2, Membranes 9 (2019) 41, https://doi.org/10.3390/membranes9030041.
[52] L.M. Robeson, The upper bound revisited, J. Membr. Sci. 320 (2008) 390–400, https://doi.org/10.1016/j.memsci.2008.04.030.
[53] B. Comesaña-Gándara, J. Chen, C.G. Bezzu, M. Carta, I. Rose, M.-C. Ferrari, E. Esposito, A. Fuoco, J.C. Jansen, N.B. McKeown, Redefining the Robeson upper bounds for CO_2/CH_4 and CO_2/N_2 separations using a series of ultrapermeable benzotriptycene-based polymers of intrinsic microporosity, Energy Environ. Sci. 12 (2019) 2733–2740, https://doi.org/10.1039/c9ee01384a.
[54] S. Shahid, K. Nijmeijer, Performance and plasticization behavior of polymer–MOF membranes for gas separation at elevated pressures, J. Membr. Sci. 470 (2014) 166–177, https://doi.org/10.1016/j.memsci.2014.07.034.